CrossMark

JM PAPERS

Modulation of turbulence intensity by heavy finite-size particles in upward channel flow

Zhaosheng Yu[1,†], **Yan Xia**[1], **Yu Guo**[1] and **Jianzhong Lin**[1]

[1]State Key Laboratory of Fluid Power and Mechatronic Systems, Department of Mechanics, Zhejiang University, Hangzhou 310027, PR China

It has been recognized that, generally, large particles enhance the turbulence intensity, while small particles attenuate the turbulence intensity. However, there has been no consensus on the quantitative criterion for particle-induced turbulence enhancement or attenuation. In the present study, interface-resolved direct numerical simulations of particle-laden turbulent flows in an upward vertical channel are performed with a direct forcing/fictitious domain method to establish a criterion for turbulence enhancement or attenuation. The effects of the particle Reynolds number (Re_p), the bulk Reynolds number (Re_b), the particle size, the density ratio and the particle volume fraction on the turbulence intensity are examined at $Re_b = 5746$ (i.e. $Re_\tau = 180.8$) and $12\,000$ ($Re_\tau = 345.9$), the ratio of the particle radius to the half channel width $a/H = 0.05$–0.15, the density ratio 2–100, the particle volume fraction 0.3 %–2.36 % and $Re_p < 227$. Our results indicate that at low Re_p the turbulent intensity across the channel is all diminished; at intermediate Re_p the turbulent intensity is enhanced in the channel centre region and attenuated in the near-wall region; and at sufficiently large Re_p the turbulent intensity is enhanced across the channel. The critical Re_p increases with increasing bulk Reynolds number, particle size and particle–fluid density ratio, while increasing with decreasing particle volume fraction, particularly for the channel centre region. Criteria for enhancement or attenuation are provided for the total turbulence intensity in the channel and the turbulence intensity at the channel centre, respectively, and both are shown to agree well with the experimental data in the literature. The reason for the dependence of the critical particle Reynolds number on the other parameters is discussed.

Key words: particle/fluid flow

† Email address for correspondence: yuzhaosheng@zju.edu.cn

1. Introduction

Particle-laden turbulent flows are commonly encountered in natural and industrial settings, such as fluidized beds, pneumatic transport, fuel combustion and sand storms. Understanding the mechanisms of and developing accurate models for multiphase turbulent flows are of great importance to better designs of relevant industrial devices. Owing to the complicated interactions between particles and turbulence, the mechanisms of turbulence modulation and their parametric dependence remain poorly understood (Balachandar & Eaton 2010). It is still not clear under what conditions the turbulence intensity is enhanced or attenuated by particles, despite extensive investigations over the past several decades (Saber, Lundström & Hellström 2015).

Numerous experiments have been reported on turbulence modulation in gas–solid flows (Lee & Durst 1982; Tsuji & Morikawa 1982; Tsuji, Morikawa & Shiomi 1984; Parthasarathy & Faeth 1990; Schreck & Kleis 1993; Kulick, Fessler & Eaton 1994; Petersen, Baker & Coletti 2019; Zhu *et al.* 2019) and liquid–solid flows (Sato & Hishida 1996; Suzuki, Ikenoya & Kasagi 2000; Kiger & Pan 2002; Kussin & Sommerfeld 2002; Hosokawa & Tomiyama 2004, 2009; Bellani *et al.* 2012; Shokri *et al.* 2017; Zade, Lundell & Brandt 2019; Mena & Curtis 2020). It has been recognized that small particles tend to attenuate the turbulence, whereas large particles enhance the turbulence (Tsuji & Morikawa 1982; Tsuji *et al.* 1984; Gore & Crowe 1989).

Gore & Crowe (1989) summarized the previous experimental data on vertical and horizontal pipe and jet flows, and suggested the ratio of the particle diameter d_p to the characteristic length scale of energy-containing eddies l_e as a critical parameter for turbulence modulation: $d_p/l_e < 0.1$ for turbulence attenuation and $d_p/l_e > 0.1$ for turbulence augmentation. Hetsroni (1989) argued that particles suppress the turbulence at low particle Reynolds numbers and enhance the turbulence at high Reynolds numbers due to vortex shedding. He took the critical Reynolds number for the turbulence augmentation as 400, considering that vortex shedding takes place at this Reynolds number. Kulick *et al.* (1994) experimentally observed in a downward channel flow that the turbulence was attenuated by small particles, and that the degree of attenuation increased with increasing particle loading and particle Stokes number. Crowe (2000) extended the criterion of Gore & Crowe (1989) from the balance between the production and dissipation of the turbulent kinetic energy at the pipe centre, and many parameters were involved, including particle volume fraction, density ratio, flow Reynolds number, Froude number, particle-free turbulence intensity, as well as d_p/l_e.

Hosokawa & Tomiyama (2004) demonstrated that the ratio of the eddy viscosity induced by the dispersed phase to the shear-induced eddy viscosity was a good parameter for correlating turbulence modification of their upward vertical pipe flows, which is defined as $u_r d_p/u'l_e$, where u_r is the average slip velocity and u' is the single-phase turbulent fluctuating velocity. Righetti & Romano (2004) showed that the particle Stokes number St (the ratio of the particle relaxation time to the characteristic time of energy-containing eddies) was a critical parameter for the particle modification of the horizontal turbulent open channel flow: turbulence augmentation at $St > 1$ and attenuation at $St < 1$. The experimental results of Noguchi & Nezu (2009) on turbulent open channel flow indicated that the turbulent intensity was enhanced when the particle diameter was larger than the zone-averaged turbulence Kolmogorov length scale. Tanaka & Eaton (2008) derived a novel dimensionless parameter, called the particle momentum number $Pa = St\,Re_L^2(\eta/L)^3$ (with Re_L being the Reynolds number based on the large-eddy length scale L and η the Kolmogorov length), using dimensional analysis of the particle force in the momentum equation. From the previous experimental data on vertical and horizontal pipe and channel

flows, the turbulence was augmented at $Pa < 10^3$ or $Pa > 10^5$, and attenuated at $10^3 < Pa < 10^5$.

With a similar dimensional analysis method, Luo, Luo & Fan (2016) derived another dimensionless parameter, Cr, defined as $Cr = (\rho_p/\rho_f)(L/d_p)Re_L^{-11/16}Re_p$ (with ρ_p, ρ_f and Re_p denoting the particle density, fluid density and particle Reynolds number, respectively), and the experimental data on vertical and horizontal pipe and channel flows indicated turbulence augmentation for $Cr > 7000$ and attenuation for $Cr < 7000$.

Some criteria for turbulence enhancement or attenuation in the literature are presented in table 1. These criteria are based on approximate theories and experimental data, which were generally scattered because of difficulty in measuring the particle-laden turbulent flow accurately.

So far, no criterion has been proposed from the numerical simulations, to the best of our knowledge. However, direct numerical simulations (DNS) with the point-particle-based and interface-resolved methods have provided deep insights into the mechanisms of turbulence modification by particles. The point-particle-based DNS have been applied to isotropic turbulent flows (Squires & Eaton 1990; Elghobashi & Truesdell 1993; Wang & Maxey 1993; Saito, Watanabe & Gotoh 2019) and turbulent channel flows (Li *et al.* 2001; Eaton 2009; Wang 2010; Zhao, Andersson & Gillissen 2010, 2013; Vreman 2015; Liu *et al.* 2017; Wang *et al.* 2019; Muramulla *et al.* 2020). In principle, the point-particle method is limited to small particles with size smaller than the Kolmogorov length scale. Therefore, turbulence attenuation was generally observed in the point-particle simulations. Squires & Eaton (1990) reported that particles weakened the large-scale structures, whereas they intensified the small-scale structures in the homogeneous isotropic turbulence.

Li *et al.* (2001) studied particle-laden gas flows in a downward channel and found that, at small mass loading, the particles tended to increase the turbulence, while they tended to suppress the turbulence at high mass loadings. Zhao *et al.* (2010, 2013) showed that, at a large Stokes number, the streamwise velocity fluctuation was increased, while the spanwise and wall-normal velocity fluctuations were decreased. The numerical results of Liu *et al.* (2017) indicated that, in a vertical channel flow, the turbulence was weakened more significantly as the Stokes number increased. Vreman (2015) demonstrated that the non-uniform part of the mean feedback force contributed significantly to the particle-induced turbulence attenuation in upward channel flow. Recently, Muramulla *et al.* (2020) observed that the turbulent kinetic energy (TKE) of upward channel flow decreased suddenly with the increase of particle volume fraction, and argued that this attenuation was caused by the decrease of the TKE generation term, instead of the increase of the turbulent dissipation rate caused by particles.

Interface-resolved direct numerical simulation (IR-DNS) is a better method to study turbulence modulation by finite-size particles with size significantly larger than the Kolmogorov length scale (Balachandar & Eaton 2010; Tenneti & Subramaniam 2014; Maxey 2017). The essential features of the interface-resolved methods are that the interfaces between the particles and the fluid are resolved and the hydrodynamic forces on the particles are determined from the solution of the flow fields outside the particle boundaries. Such methods have been applied to simulations of particle-laden isotropic homogeneous flows (Ten Cate *et al.* 2004; Lucci, Ferrante & Elghobashi 2010; Gao, Li & Wang 2013), pipe flows (Wu, Shao & Yu 2011; Peng & Wang 2019), channel flows (Kajishima *et al.* 2001; Uhlmann 2008; Garcia-Villalba, Kidanemariam & Uhlmann 2012; Shao, Wu & Yu 2012; Picano, Breugem & Brandt 2015; Santarelli & Fröhlich 2015; Wang *et al.* 2016; Yu, Vinkovic & Buffat 2016*a*; Ardekani *et al.* 2017; Yu *et al.* 2017;

Authors	Criterion parameter	Turbulence augmentation	Turbulence attenuation	Experimental data
Gore & Crowe (1989)	d_p/l_e	$d_p/l_e > 0.1$	$d_p/l_e < 0.1$	Vertical and horizontal pipe and jet flows
Hetsroni (1989)	Re_p (particle Reynolds number)	$Re_p > 400$	—	Vertical and horizontal pipe and jet flows
Hosokawa & Tomiyama (2004)	$u_r d_p/u'l_e$	$u_r d_p/u'l_e > 1$	$u_r d_p/u'l_e < 1$	Upward vertical pipe flows
Righetti & Romano (2004)	St (ratio of particle relaxation time to large-eddy time scale)	$St > 1$	$St < 1$	Horizontal open channel flow
Noguchi & Nezu (2009)	d_p/η (ratio of particle diameter to Kolmogorov time scale)	$d_p/\eta > 1$	$d_p/\eta < 1$	Horizontal open channel flow
Tanaka & Eaton (2008)	$Pa = St\, Re_L^2 (\eta/L)^3$	$Pa < 10^3$ or $Pa > 10^5$	$10^3 < Pa < 10^5$	Vertical and horizontal pipe and channel flows
Luo et al. (2016)	$Cr = (\rho_p/\rho_f)(L/d_p)Re_L^{-11/16} Re_p$	$Cr > 7000$	$Cr < 7000$	Vertical and horizontal pipe and channel flows

Table 1. Some criteria for turbulence enhancement or attenuation in the literature.

Costa *et al.* 2018; Peng, Ayala & Wang 2019; Costa, Brandt & Picano 2020; Zhu *et al.* 2020*b*), duct flows (Lin *et al.* 2017*a*, ; Fornari *et al.* 2018) and Couette flows (Wang, Abbas & Climent 2017). Lucci *et al.* (2010) observed that particles larger than the Kolmogorov scale always reduced the average TKE of the decaying homogeneous isotropic turbulence, and attributed the reason to the particle-induced viscous dissipation near particle surfaces. The finite-size particles reduced the energy spectrum of low wavenumbers and increased the energy spectrum of high wavenumbers (Lucci *et al.* 2010), similar to the point-particle case (Squires & Eaton 1990). The critical wavenumber depended not only on the actual size of the particles, but also on the relative size of the particle with respect to the turbulence scale and the density ratio (Gao *et al.* 2013).

Regarding the effects of finite-size neutrally buoyant particles on turbulent channel flow, the results of Shao *et al.* (2012) indicated that the presence of particles decreased the streamwise maximum root-mean-square (r.m.s.) velocity near the wall by weakening the intensity of the large-scale streamwise vortices, while increasing the transverse and spanwise r.m.s. velocities in the near-wall region by inducing particle-scale vortices, as later observed by Picano *et al.* (2015) and Wang *et al.* (2016). When gravity was not considered, the particles with large inertia (i.e. large density ratio) significantly suppressed the turbulence (Fornari *et al.* 2016; Yu *et al.* 2017).

Regarding horizontal channel flows, Shao *et al.* (2012) showed that sediments played the role of a rough wall and parts of the vortex structures shedding from the particles ascended into the centre region and substantially increased the turbulence intensity there. Peng *et al.* (2019) and Vreman & Kuerten (2018) studied the flow modulation by an array of fixed and moving spherical particles in turbulent channel flows, respectively, and attenuation of TKE was observed. Regarding upward channel flow loaded with heavy spherical particles, Kajishima *et al.* (2001) and Uhlmann (2008) conducted interface-resolved simulations at particle Reynolds numbers greater than 130 where the particle settling velocity was comparable to the fluid mean velocity. Both results showed that the particles strongly enhanced the turbulence intensity. Santarelli & Fröhlich (2015) simulated upward turbulent channel flow laden with spherical bubble particles at particle Reynolds numbers greater than 200, and also observed turbulence enhancement. Zhu *et al.* (2020*a*) showed that finite-size particles attenuated the turbulence in upward channel flows at relatively low particle Reynolds numbers (smaller than 33) and the increase in the particle Reynolds number (i.e. settling coefficient) gave rise to more pronounced attenuation. Therefore, for upward channel flow, there should exist a critical particle Reynolds number for the transition from turbulence attenuation to augmentation. The main aim of the present study is to determine the dependence of this critical particle Reynolds number on the control parameters, including the particle size, particle volume fraction, density ratio and channel Reynolds number. In other words, we attempt to present a new criterion for turbulence modulation, from the interface-resolved simulations of upward channel flows.

The rest of the paper proceeds as follows. The numerical method and the flow model are presented in the next section (§ 2). The accuracy of our code for the single-phase TKE budget and the collision model are validated in § 3. In § 4, the results of the particle effects on the turbulence statistics and the criteria for turbulent intensity modulation are presented. The reasons for the particle effects on the TKE are discussed in association with the modelling of the interfacial term in the TKE equation. In addition, the results on the wall friction and the total flow drag are reported. Finally, concluding remarks are given in § 5.

2. Methodology and simulation set-up

2.1. *Direct forcing/fictitious domain method*

In the present study, we employ a direct forcing/fictitious domain (DF/FD) method proposed by Yu & Shao (2007) to conduct IR-DNS of upward turbulent channel flows. The key idea of this method is that the interior of particles is filled with the fluid and the interior 'fictitious' fluid is enforced to satisfy the rigid-body motion constraint through a pseudo body force (i.e. distributed Lagrange multiplier (Glowinski *et al.* 1999)). For the simplicity of description, we consider only one particle in the following formulae. Let $P(t)$ represent the solid domain and Ω represent the entire domain including both the interior and exterior of the solid body. The particle density, volume and moment-of-inertia tensor, translational velocity and angular velocity are denoted by ρ_s, V_p, $\boldsymbol{J}$, $\boldsymbol{U}$ and $\boldsymbol{\omega}_p$, respectively. The viscosity and density of the fluid are μ and ρ_f, respectively.

We introduce the following characteristic scales for the non-dimensionalization: L_c for length, U_c for velocity, L_c/U_c for time and $\rho_f U_c^2/L_c$ for the body force. Then, the dimensionless FD formulation for the incompressible fluid can be written as

$$\frac{\partial \boldsymbol{u}}{\partial t} + \boldsymbol{u} \cdot \nabla \boldsymbol{u} = \frac{\nabla^2 \boldsymbol{u}}{Re} - \nabla p + \boldsymbol{\lambda} \text{ in } \Omega, \tag{2.1}$$

$$\boldsymbol{u} = \boldsymbol{U} + \boldsymbol{\omega}_p \times \boldsymbol{r} \text{ in } P(t), \tag{2.2}$$

$$\nabla \cdot \boldsymbol{u} = 0 \text{ in } \Omega, \tag{2.3}$$

$$(\rho_r - 1)V_p^* \left(\frac{\mathrm{d}\boldsymbol{U}}{\mathrm{d}t} - Fr\frac{\boldsymbol{g}}{g} \right) = -\int_P \boldsymbol{\lambda} \, \mathrm{d}\boldsymbol{x}, \tag{2.4}$$

$$(\rho_r - 1)\frac{\mathrm{d}(\boldsymbol{J}^* \cdot \boldsymbol{\omega}_p)}{\mathrm{d}t} = -\int_P \boldsymbol{r} \times \boldsymbol{\lambda} \, \mathrm{d}\boldsymbol{x}. \tag{2.5}$$

Here $\boldsymbol{u}$, p, $\boldsymbol{\lambda}$ and $\boldsymbol{r}$ represent the fluid velocity, pressure, pseudo body force and position vector with respect to the centre of mass of the particle, respectively, ρ_r is the particle–fluid density ratio defined by $\rho_r = \rho_s/\rho_f$, Re is the Reynolds number defined by $Re = \rho_f U_c L_c/\mu$, Fr is the Froude number defined by $Fr = gL_c/U_c^2$, with g being the gravitational acceleration, and V_p^* and $\boldsymbol{J}^*$ are the dimensionless particle volume and moment-of-inertia tensor defined by $V_p^* = V_p/L_c^3$ and $\boldsymbol{J}^* = \boldsymbol{J}/\rho_s L_c^5$.

A fractional-step time scheme is used to decouple the system (2.1)–(2.5) into the following two subproblems.

(1) Fluids subproblem for $\boldsymbol{u}^*$ and p:

$$\frac{\boldsymbol{u}^* - \boldsymbol{u}^n}{\Delta t} - \frac{1}{2}\frac{\nabla^2 \boldsymbol{u}^*}{Re} = -\nabla p - \frac{1}{2}[3(\boldsymbol{u} \cdot \nabla \boldsymbol{u})^n - (\boldsymbol{u} \cdot \nabla \boldsymbol{u})^{n+1}] + \frac{1}{2}\frac{\nabla^2 \boldsymbol{u}^n}{Re} + \boldsymbol{\lambda}^n, \tag{2.6}$$

$$\nabla \cdot \boldsymbol{u}^* = 0. \tag{2.7}$$

A finite-difference-based projection method on a homogeneous half-staggered grid is used for the solution of the above fluid subproblem. All spatial derivatives are discretized with a second-order central-difference scheme.

(2) Particle subproblem for $\boldsymbol{U}^{n+1}$, $\boldsymbol{\omega}_p^{n+1}$, $\boldsymbol{\lambda}^{n+1}$ and $\boldsymbol{u}^{n+1}$:

$$\rho_r V_p^* \frac{\boldsymbol{U}^{n+1}}{\Delta t} = (\rho_r - 1)V_p^* \left(\frac{\boldsymbol{U}^n}{\Delta t} - Fr\frac{\boldsymbol{g}}{g} \right) + \int_P \left(\frac{\boldsymbol{u}^*}{\Delta t} - \boldsymbol{\lambda}^n \right) \mathrm{d}\boldsymbol{x}, \tag{2.8}$$

$$\rho_r \frac{\boldsymbol{J}^* \cdot \boldsymbol{\omega}_p^{n+1}}{\Delta t} = (\rho_r - 1) \left[\frac{\boldsymbol{J}^* \cdot \boldsymbol{\omega}_p^n}{\Delta t} - \boldsymbol{\omega}_p^n \times (\boldsymbol{J}^* \cdot \boldsymbol{\omega}_p^n) \right] + \int_P \boldsymbol{r} \times \left(\frac{\boldsymbol{u}^*}{\Delta t} - \boldsymbol{\lambda}^n \right) \mathrm{d}\boldsymbol{x}. \quad (2.9)$$

The pseudo body force $\boldsymbol{\lambda}$ is then updated from

$$\boldsymbol{\lambda}^{n+1} = \frac{\boldsymbol{U}^{n+1} + \boldsymbol{\omega}_p^{n+1} \times \boldsymbol{r} - \boldsymbol{u}^*}{\Delta t} + \boldsymbol{\lambda}^n. \quad (2.10)$$

Finally, the fluid velocities $\boldsymbol{u}^{n+1}$ at the Eulerian nodes are corrected from

$$\boldsymbol{u}^{n+1} = \boldsymbol{u}^* + \Delta t(\boldsymbol{\lambda}^{n+1} - \boldsymbol{\lambda}^n). \quad (2.11)$$

In the above manipulations, the trilinear function is used to transfer the fluid velocity from the Eulerian nodes to the Lagrangian nodes and the pseudo body force from the Lagrangian nodes to the Eulerian nodes.

2.2. *Collision model*

A state-of-the-art collision model based on the combination of a soft-sphere collision model and the lubrication force correction has been developed for the IR-DNS by Kempe & Fröhlich (2012), Brändle de Motta *et al.* (2013), Costa *et al.* (2015) and Biegert, Vowinckel & Meiburg (2017). A similar collision model is used here. The lubrication force correction has the following form:

$$\boldsymbol{F}_{ij}^l = -6\pi\mu a \boldsymbol{u}_n [\lambda(\epsilon) - \lambda(\epsilon_{al})], \quad (2.12)$$

where $\boldsymbol{u}_n$ is the normal relative velocity between the ith and jth objects (particle or wall), $\lambda(\epsilon)$ is a function of the normalized gap distance $\epsilon = \zeta_n/a$ and $\epsilon_{al} = \Delta x/a$ is the threshold gap below which the lubrication correction is activated, where a represents the particle radius and Δx is the mesh size. The lubrication force is kept constant for $\epsilon < \epsilon_1$, where ϵ_1 is set to 0.001 in our simulations.

The functions λ for the particle–particle and particle–wall interactions are (Jeffrey 1982):

$$\text{particle–particle} \quad \lambda(\epsilon) = \frac{1}{4\epsilon} - \frac{9}{40} \ln(\epsilon) - \frac{3}{92}\epsilon \ln(\epsilon) + 0.673, \quad (2.13)$$

$$\text{particle–wall} \quad \lambda(\epsilon) = \frac{1}{\epsilon} - \frac{1}{5} \ln(\epsilon) - \frac{1}{21}\epsilon \ln(\epsilon) + 0.9713. \quad (2.14)$$

A discrete element model is employed as a soft-sphere collision model. The components of the collision force on the object i applied by another object j are (Crowe *et al.* 2011)

$$\boldsymbol{F}_{ij,n} = (-k_n \delta_n^{3/2} - \eta_n \boldsymbol{G} \cdot \boldsymbol{n})\boldsymbol{n}, \quad (2.15)$$

$$\boldsymbol{F}_{ij,t} = -k_t \boldsymbol{\delta}_t - \eta_t \boldsymbol{G}_{ct}, \quad (2.16)$$

where $\boldsymbol{F}_{ij,n}$, δ_n, k_n and η_n are the contact force, overlapping distance, stiffness coefficient and damping coefficient in the normal direction, respectively, and $\boldsymbol{F}_t$, δ_t, k_t and η_t are the corresponding parameters in the tangential direction. Here $\boldsymbol{n}$ is the unit normal vector pointing from the centre of particle i to that of particle j, $\boldsymbol{G}$ is the relative velocity between

particles and $\boldsymbol{G}_{ct}$ is the tangential relative velocity. The definitions of k_n and k_t are given by Hertzian contact theory (Hertz 1882) and Mindlin's theory (Mindlin 1953) as

$$k_n = \frac{4}{3} \left(\frac{1 - \sigma_i^2}{E_i} + \frac{1 - \sigma_j^2}{E_j} \right)^{-1} \left(\frac{a_i + a_j}{a_i a_j} \right)^{-1/2}, \tag{2.17}$$

$$k_t = 8 \left(\frac{2 - \sigma_i}{G_i} + \frac{2 - \sigma_j}{G_j} \right)^{-1} \left(\frac{a_i + a_j}{a_i a_j} \right)^{-1/2} \delta_n^{1/2}, \tag{2.18}$$

where E and σ are Young's modulus and Poisson's ratio, respectively, and $G = E/2(1 + \sigma)$ is the particle shear modulus. The damping coefficients are given by Tsuji, Tanaka & Ishida (1992) and Barnocky & Davis (1988) as

$$\eta_n = \alpha_n \sqrt{m_p k_n} \delta_n^{1/4}, \quad \eta_t = \alpha_t \sqrt{m_p k_t} \delta_t^{1/4}, \tag{2.19a,b}$$

where $m_p = m_i m_j / (m_i + m_j)$ is the effective mass and α_n is a constant related to the dry coefficient of restitution e_d as

$$\alpha_n(e_d) = \alpha_t(e_d) = 2.22 - 2.26 e_d^{0.4}. \tag{2.20}$$

If $|\boldsymbol{F}_t| \geq f |\boldsymbol{F}_n|$, the tangential force is given by the Coulomb-type friction law:

$$\boldsymbol{F}_t = -f |\boldsymbol{F}_n| \boldsymbol{t}, \tag{2.21}$$

where f is the friction coefficient and $\boldsymbol{t}$ is the unit tangential vector. In the present study, we set $E/(\rho_f u_b^2) = 2 \times 10^3$ (here u_b being the mean velocity of the channel flow), $e_d = 0.97$, $\sigma = 0.33$, and $f = 0.3$ for particle–particle collisions and $f = 0.2$ for particle–wall collisions. The time step for the collision is set to be one-tenth of that for the flow solution.

We have recently investigated the effects of the collision model on the turbulent channel flow laden with neutrally buoyant particles (Xia *et al.* 2020a). The results showed that the lubrication force correction for the particle pairs had an important effect on the particle pair statistics at the near-contact regime, and could lead to the decrease in the flow friction by around 1.4 % for a particle volume fraction of 2.36 %. For an upward channel flow laden with heavy particles here, the effect of the collision model is expected to be less significant, compared to the neutrally buoyant case, since the heavy particles tend to migrate away from the wall and there are fewer particles in the near-wall region where the particles would collide more frequently and strongly due to high shear rates.

2.3. *Simulation set-up*

The schematic diagram of the upward channel flow is delineated in figure 1. The computational domain is $[0, 8H] \times [-H, H] \times [0, 4H]$ in the streamwise (x), wall-normal (y) and spanwise (z) directions, where H is the half channel width. A periodic boundary condition is imposed in the streamwise and spanwise directions, and the no-slip condition is imposed on the sidewalls.

The flow is driven upwards by a mean pressure gradient $-\mathrm{d}p_e/\mathrm{d}x$ in the direction of the x coordinate to maintain a constant flow rate. The pressure gradient is varied as the particle parameters are changed. We choose H and the bulk velocity u_b as the characteristic length and velocity. The channel Reynolds number is defined as $Re_b = u_b(2H)/\nu$, where ν is the fluid kinematic viscosity; Re_b is constant in the simulations, since the bulk velocity u_b is kept constant. Finally, $\boldsymbol{g} = (-g, 0, 0)$ is the vector of gravitational acceleration.
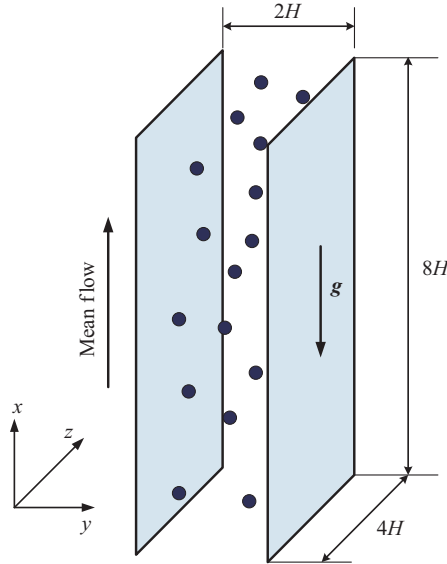
Figure 1. Schematic diagram of the upward channel flow laden with particles; with x, y and z representing the streamwise, transverse and spanwise coordinates, respectively.

We introduce a dimensionless parameter u_i/u_b as the settling coefficient to control the particle settling effect, where u_i is the velocity of a particle settling in a quiescent fluid when the standard drag coefficient is unity, defined by

$$u_i = \sqrt{\frac{8a}{3}(\rho_r - 1)g}. \qquad (2.22)$$

Since the terminal velocity of a sphere settling in an unbounded domain is $u_T = \sqrt{(1/C_D)(8a/3)(\rho_r - 1)g}$, where C_D represents the standard drag coefficient, u_i is related to u_T via

$$\frac{u_T}{u_i} = \sqrt{\frac{1}{C_D}}. \qquad (2.23)$$

For a relatively strong fluid inertial effect, u_i is close to u_T, since the drag coefficient is close to unity.

The Galileo number, defined as $Ga = \sqrt{8a^3(\rho_r - 1)g}/\nu$ (with ν being the fluid kinematic viscosity), is widely used to measure the particle settling effect. The particle Reynolds number based on u_i is related to the Galileo number via $Re_i = u_i(2a)/\nu = \sqrt{4/3}Ga$. We note that the Archimedes number is the square of the Galileo number, and Re_i^2 was defined as the 'best number' for the particle settling problem (Yu, Phan-Thien & Tanner 2004; Clift, Grace & Weber 2005). For a given value of u_i/u_b, the Galileo number can be computed by

$$Ga = \frac{\sqrt{3}}{2}\frac{a}{H}\frac{u_i}{u_b}Re_b. \qquad (2.24)$$

The Froude number Fr can be determined from other control parameters:

$$Fr = \frac{gH}{u_b^2} = \frac{3(u_i/u_b)^2}{8(a/H)(\rho_r - 1)}. \qquad (2.25)$$

913 A3-9

Group no.	a/H	$N_x \times N_y \times N_z$	Re_b	ρ_s/ρ_f	N_p	Φ_0 (%)
1	0.1	$512 \times 128 \times 256$	5746	2.0	360	2.36
2	0.1	$512 \times 128 \times 256$	5746	10.0	360	2.36
3	0.1	$512 \times 128 \times 256$	5746	100.0	360	2.36
4	0.1	$512 \times 128 \times 256$	5746	2.0	360	0.84
5	0.05	$1024 \times 256 \times 512$	5746	2.0	2880	2.36
6	0.05	$1024 \times 256 \times 512$	12 000	2.0	2880	2.36
7	0.05	$1024 \times 256 \times 512$	5746	2.0	360	0.30
8	0.075	$1024 \times 256 \times 512$	5746	2.0	853	2.36
9	0.15	$512 \times 128 \times 256$	5746	2.0	107	2.36

Table 2. Parameter settings for the particle-laden flows in a vertical channel: a represents the radius of particles, N_p is the number of particles and Φ_0 is the mean particle volume fraction in the entire channel.

The turbulent kinetic energy of the particle-laden channel flow k is controlled by the following eight parameters (seven dimensional and one dimensionless): $k = f(u_b, H, a, \rho_s, \rho_f, \mu, g, N_p)$, where N_p represents the number of particles in the system. Accordingly, the dimensionless turbulent kinetic energy should be a function of five dimensionless parameters and we choose them as $k/u_b^2 = f(Re_b, a/H, \rho_r, u_i/u_b, \Phi_0)$, where Φ_0 is the mean particle volume fraction in the entire channel. Since the particle wake is more closely related to the particle Reynolds number Re_p than the settling coefficient, the settling coefficient is replaced with Re_p in the criterion for turbulence enhancement. Note that the particle Reynolds number is based on the average slip velocity between the two phases at the channel centre: $Re_p = |\langle u_f \rangle - \langle u_p \rangle| 2a/\nu$, where $\langle u_f \rangle$ and $\langle u_p \rangle$ are the average velocities of the fluid and particles at the channel centre, respectively.

To examine the effects of the particle size, particle volume fraction, channel Reynolds number and density ratio, nine groups of parameters are chosen. For each group, the settling coefficient u_i/u_b is varied to determine the critical particle Reynolds number for turbulence augmentation. We note that when the other parameters (Re_b, a/H, ρ_r) are fixed, the settling coefficient is varied by changing the gravitational acceleration, which we have chosen as the dimensional control parameter. The parameter settings for the nine groups are presented in table 2. There are in total 61 cases, with the consideration of different values of u_i/u_b for each group (see tables 6 and 7).

Two channel Reynolds numbers $Re_b = 5746$ and 12 000 are considered, corresponding to the friction Reynolds numbers $Re_\tau = \rho_f u_\tau H/\mu = 180.8$ and 345.9 for the single-phase flow, respectively, as listed in table 6. Here, u_τ is the friction velocity, defined by $u_\tau = \sqrt{\tau_w/\rho_f}$, where τ_w represents the mean wall shear stress. The Kolmogorov length η for the turbulent channel flow can be computed by

$$\frac{\eta}{H} = \frac{1}{H}\left(\frac{\nu^3}{\varepsilon}\right)^{1/4} = \frac{1}{H}\left(\frac{\nu^3}{\varepsilon^*(u_b^3/H)}\right)^{1/4} = \left(\frac{1}{\varepsilon^*(Re_b/2)^3}\right)^{1/4},$$

where ν is the kinematic viscosity, ε is the turbulence dissipation rate and ε^* is the dimensionless turbulence dissipation rate normalized with u_b^3/H. The Taylor microscale can be defined as $\lambda = \sqrt{15\nu u'^2/\varepsilon} = \sqrt{10\nu k/\varepsilon}$, where u' is the turbulence intensity, related to the turbulent kinetic energy via $k = 3u'^2/2$ (Gao *et al.* 2013). The Taylor-microscale Reynolds number is defined by $Re_\lambda = u'\lambda/\nu$, and it can be derived that $Re_\lambda = \sqrt{(10/3)(k^*)^2 Re_b/\varepsilon^*}$, where k^* is the dimensionless turbulent kinetic energy

913 A3-10

normalized by u_b^2. From our simulations, $k^* = 2.86 \times 10^{-3}$ and $\varepsilon^* = 2.52 \times 10^{-4}$ for $Re_b = 5746$, and $k^* = 2.32 \times 10^{-3}$ and $\varepsilon^* = 1.89 \times 10^{-4}$ for $Re_b = 12\,000$ at the channel centre. Thus, the Kolmogorov length scale at the channel centre $\eta/H = 0.02$ for $Re_b = 5746$ and $\eta/H = 0.0125$ for $Re_b = 12\,000$. The particle size in the present study ranges from $a/H = 0.05$ to $a/H = 0.15$, corresponding to $a/\eta = 2.5$–7.5 for $Re_b = 5746$ and $a/\eta = 4$–12 for $Re_b = 12\,000$. The Taylor-microscale Reynolds number Re_λ at the channel centre is around 25 for $Re_b = 5746$ and 33.8 for $Re_b = 12\,000$, respectively.

Two mesh resolutions with respect to the particle size, $d_p/\Delta x = 12.8$ and 19.2, are used in our simulations, which are comparable to those employed by Uhlmann (2008) and Santarelli & Fröhlich (2015). The accuracy of our DF/FD code for the single-phase turbulent channel and duct flows were validated in Yu *et al.* (2016*b*, 2019) and Lin *et al.* (2017*a*). Zhu *et al.* (2020*b*) showed that the turbulence statistics for a vertical particle-laden channel flow obtained from $d_p/\Delta x = 12.8$ were in good agreement with those from $d_p/\Delta x = 25.6$. Our DF/FD code has been applied to various types of particle-laden turbulent flows, including pipe flows (Wu *et al.* 2011), duct flows (Lin *et al.* 2017*a*,) and channel flows laden with spherical particles (Shao *et al.* 2012; Yu *et al.* 2017; Xia, Yu & Guo 2020*b*) and spheroidal particles (Zhu, Yu & Shao 2018; Zhu *et al.* 2020*a*). Thus, we will only validate our codes for the single-phase mean TKE equation and the collision model later. We note that our mesh resolution in table 2 may not ensure that the solution of all turbulent flow details is highly accurate, such as the turbulent dissipation rate in the immediate vicinity of the wall or particle surfaces. However, according to our previous validation tests (Yu *et al.* 2016*b*; Zhu *et al.* 2020*b*), the mesh resolution should be sufficient for the statistical properties of large numbers of particles suspended in a turbulent flow, and their influence on the overall dynamics, which are of interest in the present study. Mesh refinement is limited by our computer resources.

The dimensionless time step is $\Delta t = 0.001$. The statistics are obtained from the averaging of the data over a period of 500 non-dimensional time units (H/u_b) after the statistically steady state is reached. The particle-phase statistics are obtained from the data at the fictitious fluid domain (i.e. the solid domain).

2.4. *Definition of turbulence intensity modulation*

The turbulence intensity modulation is quantified as the relative change in the turbulence intensity due to the presence of particles (Gore & Crowe 1989):

$$CT = \frac{I - I_{\mathrm{sp}}}{I_{\mathrm{sp}}}, \tag{2.26}$$

where I denotes the mean turbulent intensity of the fluid phase defined as $I = \sqrt{\frac{1}{3}({u'_{rms}}^2 + {v'_{rms}}^2 + {w'_{rms}}^2)}/u_b$ and the subscript 'sp' stands for the case of 'single-phase' flow. We normalize the turbulent intensity with the bulk velocity u_b, because u_b is kept constant and is the velocity scale in our computations. The velocity at the pipe centreline was typically used to normalize the turbulent intensity in the experiments (Gore & Crowe 1989). We consider the change of the turbulent intensity at the channel centre and that of the total turbulent intensity in the channel:

$$\widetilde{CT} = \frac{\displaystyle\int_{-H}^{H} (I - I_{\mathrm{sp}})\,\mathrm{d}y}{\displaystyle\int_{-H}^{H} I_{\mathrm{sp}}\,\mathrm{d}y}. \tag{2.27}$$
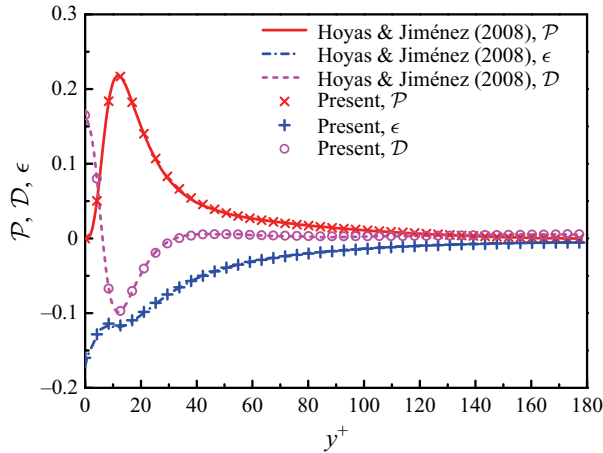
913 A3-11

Figure 2. Profiles of the mean TKE production, dissipation and diffusion terms for the particle-free turbulent channel flow, normalized with $(u_\tau)^4/\nu$, as compared to the results of Hoyas & Jiménez (2008).

We use the tilde bar $\tilde{\cdot}$ to indicate the averaging of a quantity over the entire channel in the present study.

3. Validation

The accuracy of our method for the single-phase mean and r.m.s. velocities and the mesh independence of the turbulence statistics for the particle-laden channel flow have been demonstrated in our previous works (Yu *et al.* 2016*b*, 2019; Zhu *et al.* 2020*b*). Here, we provide additional validations for the computation of the single-phase TKE equation and the collision model with the lubrication force correction, since neither has been reported previously.

3.1. *Single-phase turbulent channel flow*

The first test problem is the particle-free turbulent channel flow at $Re_\tau = 180$; here Re_τ is the friction Reynolds number defined by $Re_\tau = (\rho_f u_\tau H)/\mu$, where $u_\tau = \sqrt{\tau/\rho_f}$, with τ being the mean wall shear stress. The computational domain is $[8H \times 2H \times 4H]$, with the grid number of $1024 \times 256 \times 512$. Our profiles of the production, dissipation and diffusion terms are compared to those of Hoyas & Jiménez (2008) in figure 2. The results of Hoyas & Jiménez (2008) were obtained using the pseudo-spectral simulations with a computational domain of $12\pi H \times 2H \times 4\pi H$. From figure 2, our results are in excellent agreement with those of Hoyas & Jiménez (2008).

3.2. *Collision of a sphere with a wall in a viscous fluid*

The bouncing motion of a sphere colliding with a planar wall in a viscous fluid is numerically simulated with our fictitious domain method and the collision model presented earlier. Our results are compared to the experimental results of Gondret, Lance & Petit (2002) for two Stokes numbers $St_c = 27$ and 152. The Stokes number is defined as $St_c = \rho_s u_{in} d_p/9\mu$, with u_{in} being the impact velocity before the collision. The parameters are summarized in table 3. The trajectories of the sphere for the two cases are plotted in figure 3. Our results are in excellent agreement with the experiments.

913 A3-12

Case	St_c	ρ_s/ρ_f	e_d	Domain	Grid cells
A	27	8.08	0.97	$12d_p \times 24d_p \times 12d_p$	$256 \times 512 \times 256$
B	152	8.34	0.97	$6d_p \times 48d_p \times 6d_p$	$128 \times 1024 \times 128$

Table 3. Parameter settings for the bouncing motion of a sphere colliding with a planar wall in a viscous fluid.
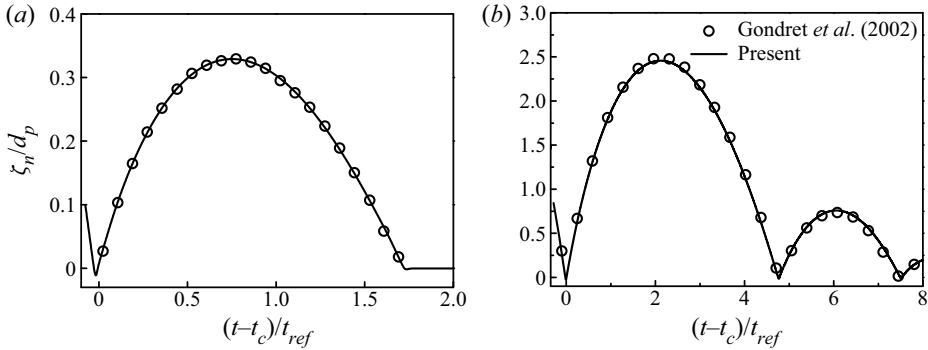

Figure 3. Trajectories of a sphere colliding with a planar wall in a viscous fluid for (*a*) $St_c = 27$ and (*b*) $St_c = 152$, compared to the experimental results of Gondret *et al.* (2002). Here ζ_n is the shortest distance between the sphere surface and the wall, and $t_{ref} = \sqrt{d_p/g}$ denotes the reference time scale.

4. Results and discussion

In this section, we first present and discuss the results on the fluid mean velocity, fluctuating velocity, vortex structure and particle concentration distribution at different settling coefficients u_i/u_b for a typical case of $a/H = 0.05$, $\Phi_0 = 2.36\,\%$, $Re_b = 5746$ and $\rho_r = 2.0$ (i.e. group 5 in table 2). Next, we examine the dependence of the critical Reynolds number on the particle size, particle volume fraction, density ratio and channel Reynolds number, report new criteria for the turbulence modulation, and analyse the mechanisms from the TKE production in the particle-laden turbulent flow. Finally, the friction drag and the total flow drag are reported. Note that, although y is defined as the coordinate in the wall-normal direction, ranging from $-H$ to H (or -1 to 1 for its dimensionless value), as used in figure 10, for convenience it is also defined as the distance away from the wall when plotting and discussing the profiles of the statistics.

4.1. *Effects of settling coefficient*

The effects of the settling coefficient on the fluid and particle statistics are investigated for the case of group 5: $a/H = 0.05$, $\Phi_0 = 2.36\,\%$, $Re_b = 5746$ and $\rho_r = 2$. The settling coefficient u_i/u_b ranges from 0.092 to 0.7. The cases of $u_i/u_b = 0.092$ and 0.159 have been studied by Zhu *et al.* (2020*a*), where the settling coefficient was defined as the ratio of the Stokes settling velocity and the bulk velocity u_s/u_b, and these two cases correspond to $u_s/u_b = 0.1$ and 0.3.

4.1.1. *Mean velocity*

Figure 4 shows the mean fluid velocity profiles, with the inset showing the close-up of the velocities in the immediate vicinity of the wall. The mean velocity profile becomes flatter as u_i/u_b increases from zero to 0.25. The mean velocity at $u_i/u_b = 0.25$ becomes
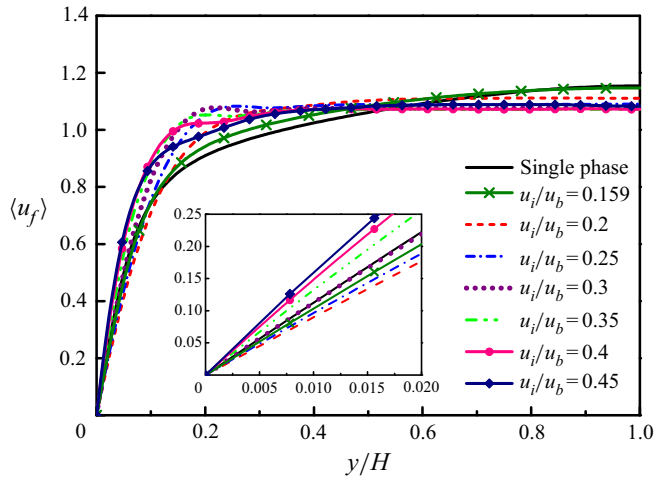
Figure 4. Mean fluid velocity profiles of turbulent channel flows for different u_i/u_b at $a/H = 0.05$, $\Phi_0 = 2.36\%$, $Re_b = 5746$ and $\rho_r = 2.0$. The inset shows the close-up of the velocity profiles near the wall.

uniform for $y > 0.3H$. As u_i/u_b further increases, the mean velocity profile remains flat in the bulk region, but at y around $0.2H$ the velocity decreases. We suspect that this decrease is related to the local peak of the particle concentration distribution, which could cause a larger local flow drag. Figure 6 shows a local peak of the particle concentration distribution at $y \approx 0.2H$ for $u_i/u_b = 0.4$.

It was shown that the presence of neutrally buoyant finite-size particles generally leads to drag enhancement (Shao *et al.* 2012; Picano *et al.* 2015; Wang *et al.* 2016). However, heavy particles in upward channel flow could cause a decrease in the wall friction at $u_i/u_b = 0.159$ due to the suppression of large-scale vortices (Zhu *et al.* 2020*a*). From the inset of figure 4, the velocity gradient on the wall (i.e. flow friction) reaches a minimum at $u_i/u_b = 0.2$, and it starts to increase as u_i/u_b increases beyond 0.2. The reason for this increase will be discussed later.

Figure 5 depicts the profiles of the fluid relative mean velocity $\langle u_f \rangle$ with respect to the particle mean velocity $\langle u_p \rangle$ (i.e. mean slip velocity), where the angle brackets denote the phase averaging. It was observed experimentally and numerically that the mean velocity of heavy particles was smaller than the fluid counterpart in the bulk region, but larger than the fluid counterpart near the wall (Tsuji *et al.* 1984; Shokri *et al.* 2017; Zhu *et al.* 2020*a*). The reason for the larger particle mean velocity near the wall was attributed to the facts that the particles can slip on the wall and are preferentially located in the high-speed streaks (Tsuji *et al.* 1984; Zhu *et al.* 2020*a*). Figure 5 shows negative slip velocities in the near-wall region at $u_i/u_b = 0.159$ and 0.2. For $u_i/u_b \geq 0.25$, there are very few particles in the region of negative slip velocity due to the migration of the particles away from the wall (see figure 6); thus the expected negative slip velocities are not plotted. The position of zero mean slip velocity shifts towards the wall, as the settling coefficient increases. Two facts might be responsible for this observation. Firstly, the preferential distribution of the heavy particles in the high-speed streaks is caused by the entrainment of the large-scale streamwise vortices from the bulk region to the near-wall region under the condition of a higher particle concentration closer to the channel centre, as illustrated by Zhu *et al.* (2020*a*) for $u_i/u_b = 0.159$. At $u_i/u_b \geq 0.25$, shear-induced large-scale vortices are significantly suppressed (see figure 10) and the particles are distributed largely
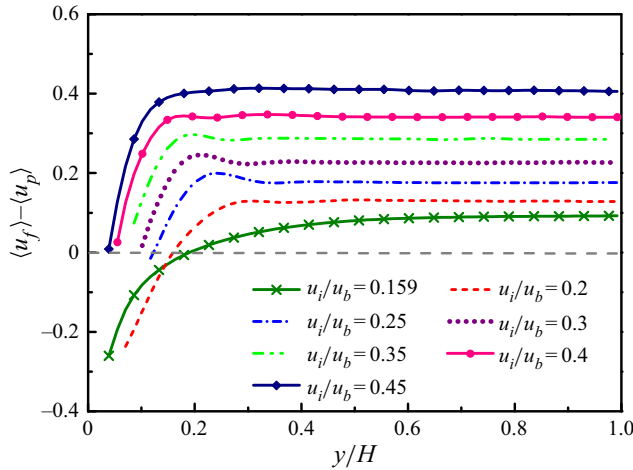
913 A3-14

Figure 5. Differences between the fluid and solid mean velocities at $a/H = 0.05$, $\Phi_0 = 2.36\%$, $Re_b = 5746$ and $\rho_r = 2.0$.
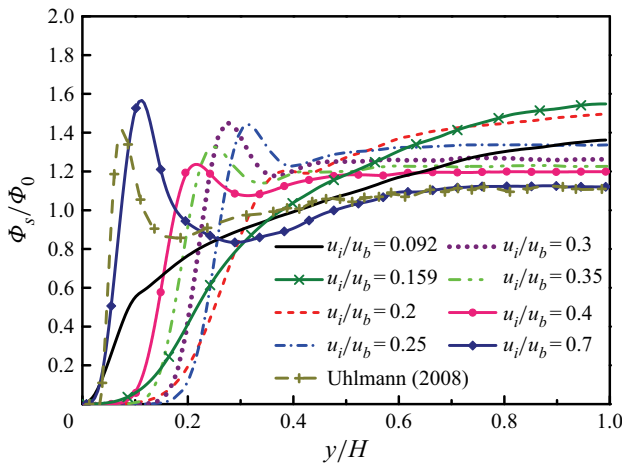

Figure 6. Profiles of the particle volume fraction at $a/H = 0.05$, $\Phi_0 = 2.36\%$, $Re_b = 5746$ and $\rho_r = 2.0$. The numerical result of Uhlmann (2008) for $a/H = 0.025$, $\Phi_0 = 0.42\%$ and $Re_p \approx 136$ is shown for comparison.

uniformly in the bulk region. Thus the preferential distribution of the heavy particles in the high-speed streaks only occurs in the near-wall region for high settling coefficients. Secondly, a larger settling coefficient itself means a larger positive slip velocity, and it also means a larger particle Reynolds number and thereby larger particle inertia. Consequently, at a larger u_i/u_b, particles with upward velocity smaller than the mean fluid velocity can approach closer to the wall.

The mean particle volume fraction, Φ_s/Φ_0, as a function of the wall-normal distance y/H is depicted in figure 6. The particle migration towards the channel (or pipe) centre was observed in numerical simulations (Zhu *et al.* 2020*a*,) and in experiments (Goes Oliveira, van der Geld & Kuerten 2017; Shokri *et al.* 2017) when the particle settling effect was not strong, as a result of the Saffman effect (Saffman 1965; Auton 1987; Auton, Hunt & Prud'Homme 1988). Costa *et al.* (2020) showed that there exists a strong shear-induced

lift force acting on the low-inertia particles in the near-wall region in turbulent channel flow and this lift force was well captured by the Saffman model, even though there was no gravity effect. As mentioned earlier, at $u_i/u_b \geq 0.25$ the particle concentration distribution is almost uniform in the bulk region, and a peak appears in the near-wall region. In fact, the peak position for $0.25 \leq u_i/u_b \leq 0.4$ is not so close to the wall, and it is around $y \approx 0.3H$ at $u_i/u_b = 0.25$. In the near-wall region, a high shear rate always exists, and a larger slip velocity causes a larger Saffman lift force, which leads to a very small particle volume fraction near the wall and the aforementioned peak. The peak position shifts closer to the wall as u_i/u_b increases. The reason should be related to larger particle inertia at a higher settling coefficient.

It is interesting that the peak position is well correlated with the trough (local minimum) of the particle r.m.s. velocity component in the wall-normal direction, from the comparison between figure 6 and figure 9(*b*). Hence, the peak of the particle concentration distribution may also be related to turbophoresis, which drives the particles from the region of high turbulent intensity to that of low turbulent intensity (Caporaloni *et al.* 1975; Reeks 1983). The mean momentum equation in the wall-normal (i.e. y) direction for the particle phase at the statistically steady state from the spatial averaging theorem (Crowe *et al.* 2011) can be written as

$$\partial(\Phi_s\langle\sigma_s\rangle_{yy})/\partial y - \partial(\Phi_s\rho_s\langle v_s'v_s'\rangle)/\partial y + \bar{F}_y = 0, \tag{4.1}$$

where σ_s denotes the particle inner (Cauchy) stress and $\bar{F}_y$ is the volume-averaged hydrodynamic force on the particles in the y direction. The particle r.m.s. velocity in the wall-normal direction (the second term in the above equation) plays a role in the force balance, similar to the fluid Reynolds stress for the fluid phase. It is also possible that the peak of the particle concentration results in the occurrence of the local minimum of the particle r.m.s. velocity.

The particle concentration distribution obtained by Uhlmann (2008) for $a/H = 0.025$ and $Re_p \approx 136$ is plotted in figure 6 for comparison. The two results for high slip velocities are qualitatively similar. The peak position of Uhlmann (2008) is closer to the wall, because his particle size is smaller than ours. As shown in figure 19, the peak position is closer to the wall for smaller particles.

4.1.2. *Fluctuating velocity and turbulent kinetic energy*

The r.m.s. values of the fluid velocity fluctuations and the Reynolds shear stress for different settling coefficients are depicted in figure 7. The r.m.s. velocities do not change monotonically as u_i/u_b increases from zero to 0.45. The addition of the particles decreases all r.m.s. velocity components across the channel at $u_i/u_b = 0.159$. At $u_i/u_b \geq 0.2$, the streamwise r.m.s. velocity at the channel centre is enhanced, whereas the wall-normal and spanwise r.m.s. velocities are attenuated across the channel at $u_i/u_b \leq 0.4$, and begin to exceed the single-phase values at the channel centre for $u_i/u_b \geq 0.45$. There is a local minimum in the profile of each r.m.s. velocity component for $0.25 \leq u_i/u_b \leq 0.4$ in figure 7, and we attribute the reason to the effect of the peak of the particle concentration distribution in figure 6. The Reynolds stress profiles for the particle-free and particle-laden cases are compared in figure 7(*d*). The Reynolds stress decreases as u_i/u_b increases up to around 0.25, and then it increases with increasing u_i/u_b, although it is still much smaller than the single-phase value at $u_i/u_b = 0.45$.

Figure 8 shows the profiles of TKE and its relative change with respect to the single-phase flow. Turbulence suppression across the entire channel is observed for $u_i/u_b \leq 0.25$. For $u_i/u_b > 0.25$, TKE augmentation in the bulk region and attenuation in
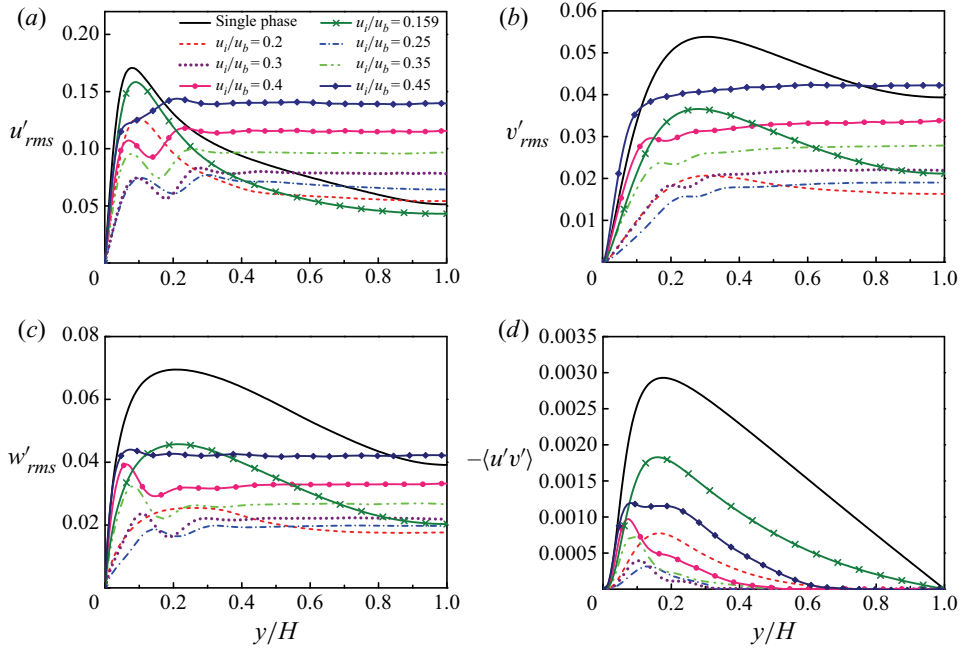
Figure 7. Profiles of the r.m.s. velocity in single-phase and particle-laden turbulent channel flows: (a) streamwise, (b) wall-normal, (c) spanwise and (d) Reynolds shear stress $-\langle u'v' \rangle$ at $a/H = 0.05$, $\Phi_0 = 2.36\%$, $Re_b = 5746$ and $\rho_r = 2.0$.
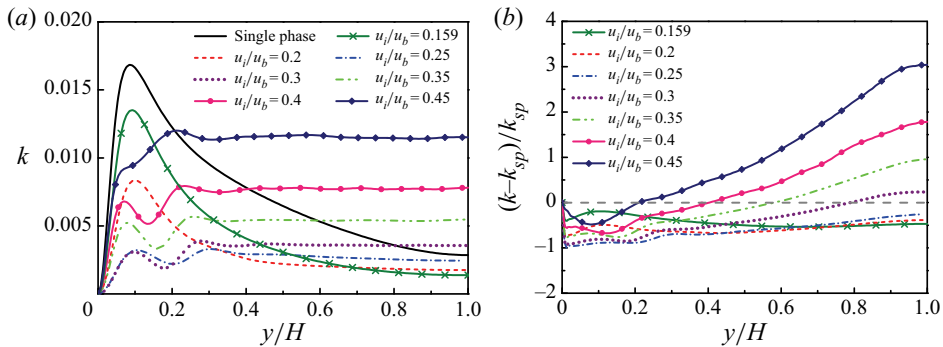

Figure 8. Profiles of (a) the TKE in single-phase and particle-laden turbulent channel flows and (b) the relative change of the TKE with respect to the single-phase flow, i.e. $(k - k_{sp})/k_{sp}$, at $a/H = 0.05$, $\Phi_0 = 2.36\%$, $Re_b = 5746$ and $\rho_r = 2.0$.

the near-wall region can be observed in figure 8, as also observed in previous experiments (Tsuji *et al.* 1984; Hosokawa & Tomiyama 2004; Mena & Curtis 2020). As u_i/u_b increases, the region for turbulence enhancement is expanded. At $u_i/u_b = 0.5$, TKE is enhanced across the entire channel (not shown in figure 8 for convenience of presentation). From table 4, the relative increase in the total TKE at $u_i/u_b = 0.5$ reaches 173.7 %.

In table 4, the average fluid-phase r.m.s. velocity components, turbulence intensity $\tilde{I}$ and TKE $\tilde{k}$ in the entire channel for $u_i/u_b \leq 0.5$ are presented. We see that the average r.m.s. velocities in all three directions, the mean turbulence intensity and the mean TKE are attenuated at $u_i/u_b \leq 0.3$, with the maximum attenuation at $u_i/u_b = 0.25$. The mean TKE

913 A3-17

u_i/u_b	Re_p	$\widetilde{u'_{rms}}$	$\widetilde{v'_{rms}}$	$\widetilde{w'_{rms}}$	$\tilde{I}$	$\tilde{k}$
SP	—	0.088	0.044	0.055	0.068	0.007
0.092	9.5	0.085 (−3.4 %)	0.041 (−6.8 %)	0.052 (−5.5 %)	0.064 (−5.7 %)	0.006 (−10.1 %)
0.159	25.6	0.071 (−17.5 %)	0.029 (−37.5 %)	0.034 (−37.4 %)	0.051 (−23.8 %)	0.004 (−40.9 %)
0.2	35.3	0.068 (−21.1 %)	0.018 (−61.8 %)	0.021 (−62.7 %)	0.044 (−34.9 %)	0.003 (−57.9 %)
0.25	49.6	0.061 (−29.6 %)	0.016 (−64.7 %)	0.017 (−68.5 %)	0.039 (−39.4 %)	0.002 (−68.6 %)
0.3	64.0	0.077 (−10.8 %)	0.020 (−55.6 %)	0.021 (−61.0 %)	0.048 (−29.9 %)	0.003 (−49.9 %)
0.35	80.1	0.095 (+9.8 %)	0.026 (−42.9 %)	0.027 (−50.3 %)	0.059 (−13.5 %)	0.005 (−23.5 %)
0.4	96.6	0.111 (+29.0 %)	0.033 (−28.5 %)	0.034 (−38.7 %)	0.071 (+4.4 %)	0.008 (+9.7 %)
0.45	113.5	0.136 (+55.1 %)	0.039 (−11.1 %)	0.041 (−25.1 %)	0.090 (+32.6 %)	0.011 (+60.2 %)
0.5	131.9	0.177 (+101.2 %)	0.053 (+20.7 %)	0.057 (+2.8 %)	0.117 (+71.8 %)	0.019 (+173.7 %)

Table 4. The average fluid-phase r.m.s. velocity components, turbulence intensity $\tilde{I}$ and TKE $\tilde{k}$ in the entire channel. The values in parentheses represent the relative differences with respect to the single-phase flow. Here Re_p is the particle Reynolds number based on mean inter-phase slip velocity at the channel centre at $a/H = 0.05$, $\Phi_0 = 2.36\,\%$, $Re_b = 5746$ and $\rho_r = 2.0$.

is enhanced for $u_i/u_b \geq 0.4$, corresponding to $Re_p \geq 96.6$. At $u_i/u_b = 0.4$ and 0.5, the increase in the mean TKE is caused by the increase in the streamwise r.m.s. velocity, since the wall-normal and spanwise r.m.s. velocities are reduced, compared to the single-phase flow. As u_i/u_b exceeds 0.5, all components of the average r.m.s. velocities are augmented by the particles.

The solid-phase r.m.s. velocities and kinematic Reynolds shear stresses $(-\langle u'_p v'_p \rangle$ without the density) are plotted in figure 9. The streamwise solid-phase r.m.s. velocities are smaller than those of the fluid in the unladen case for $u_i/u_b < 0.35$, and the wall-normal r.m.s. velocities are larger than those of the fluid in the near-wall region due to the collision between the particles and the wall. The solid-phase r.m.s. velocities generally decrease with increasing u_i/u_b for small u_i/u_b, and then increase with increasing u_i/u_b, consistent with the results of the fluid r.m.s. velocities in figure 7. As mentioned earlier, the trough (local minimum) in the profile of the wall-normal r.m.s. velocity is correlated with the peak of particle volume fraction in figure 6.

4.1.3. *Vortex structure*

Figure 10 shows the typical vortex structures in the half channel, identified with the Q criterion ($Q = 1.5$), which is defined as

$$Q = \tfrac{1}{2}(\Omega_{ij}\Omega_{ij} - S_{ij}S_{ij}), \qquad (4.2)$$

where $\Omega_{ij} = (u_{i,j} - u_{j,i})/2$ and $S_{ij} = (u_{i,j} + u_{j,i})/2$ are the fluid rotation-rate tensor and the strain-rate tensor, respectively. Zhu *et al.* (2020a) showed that the large-scale vortices were weakened more significantly at $u_i/u_b = 0.159$ than at $u_i/u_b = 0.092$. From figure 10(b), at $u_i/u_b = 0.25$ with the particle Reynolds number being approximately 50, the large-scale vortices appear to be completely suppressed. The suppression of the large-scale vortices is clearly responsible for the pronounced attenuation of the turbulence intensity at relatively small settling coefficients, as observed in figures 7 and 8, and table 4.

The reason for the suppression of the large-scale vortices is related to the effects of the drag force, the enhanced viscous dissipation, or the particle-induced wake structures. These three factors are interrelated, since a higher settling coefficient implies a larger drag
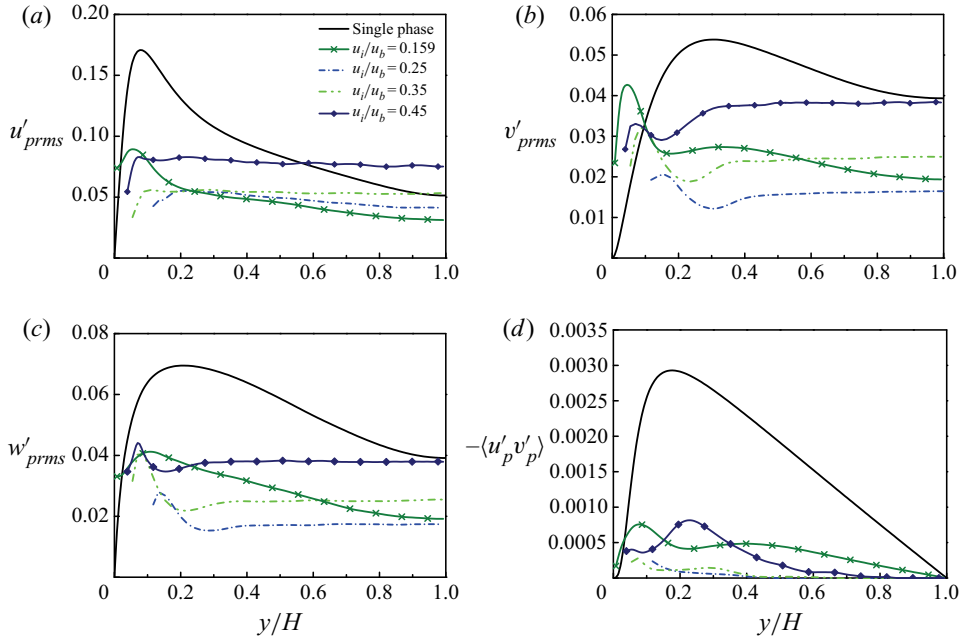
913 A3-18

Figure 9. Profiles of the r.m.s. velocity and Reynolds shear stress for the particle phase: (*a*) streamwise, (*b*) wall-normal, (*c*) spanwise and (*d*) the particle kinematic Reynolds shear stress $-\langle u'_p v'_p \rangle$ at $a/H = 0.05$, $\Phi_0 = 2.36\,\%$, $Re_b = 5746$ and $\rho_r = 2.0$.
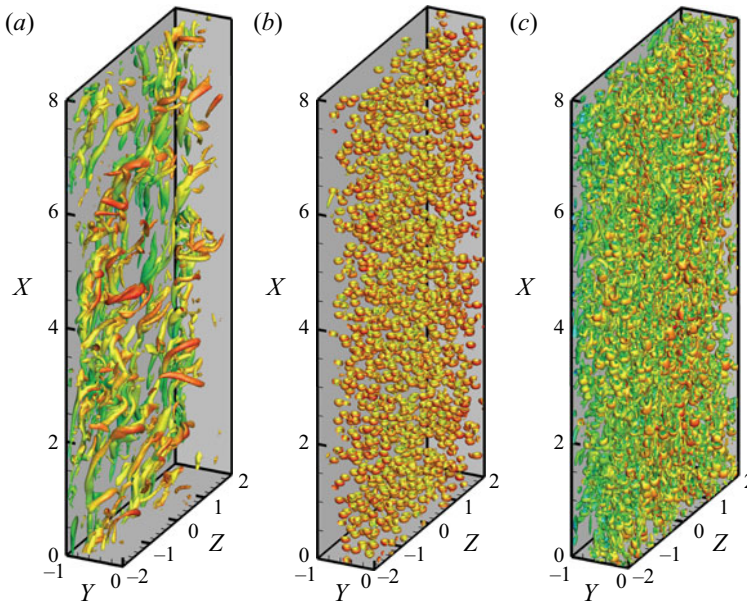

Figure 10. Vortex structures of the (*a*) single-phase flow and (*b*,*c*) the particle-laden flows for (*b*) $u_i/u_b = 0.25$ and (*c*) $u_i/u_b = 0.45$ at $a/H = 0.05$, $\Phi_0 = 2.36\,\%$, $Re_b = 5746$ and $\rho_r = 2.0$. The colour of the vortices represents the fluid streamwise velocity, with the same scale for all three cases.

force, a higher viscous dissipation and stronger particle wakes. It is not clear which effect is more important. Significant suppression of the large-scale vortices was observed in the numerical simulations based on the point-particle model (Vreman 2015; Muramulla *et al.* 2020). Vreman (2015) demonstrated that the non-uniform part of the mean feedback drag force contributed significantly to particle-induced turbulence attenuation. Xia, Yu & Deng (2019) observed that, at the same settling coefficient, light (bubble) particles attenuated the turbulence in a downward channel flow, where the particles migrated towards the channel centre, whereas light particles enhanced the turbulence in an upward channel, where the particles migrated towards the channel wall. From these observations, it seems that the particle feedback force distributed in the bulk region suppresses the self-generation of large-scale vortices in the channel flow. On the other hand, the particle wakes tend to enhance the turbulence intensity when they are sufficiently strong. Figure 10 shows strong particle wakes at $u_i/u_b = 0.45$, corresponding to $Re_p = 113.5$, in which case the intensity of the particle-induced turbulence becomes stronger than that of large-scale-vortex-induced single-phase turbulence in the bulk region, as shown in figure 8. The stronger particle wakes at a higher u_i/u_b in the near-wall region where the velocity gradient is large are expected to be responsible for the increase in the fluid Reynolds stress with increasing u_i/u_b at $u_i/u_b > 0.25$ in figure 7(*d*).

4.2. *Criterion for turbulence modulation*

4.2.1. *Effects of other parameters on TKE*

We have shown that there is a transition from turbulence attenuation to augmentation as the settling coefficient increases for the typical case of $a/H = 0.05$, $\Phi_0 = 2.36\%$, $Re_b = 5746$ and $\rho_r = 2.0$ (i.e. group 5). The TKE of the particle-laden flow starts to exceed that of the single-phase flow at the channel centre at $u_i/u_b = 0.3(Re_p = 64)$ (figure 8), while the augmentation in the total TKE starts at $u_i/u_b = 0.45$ ($Re_p = 96.6$) (table 4). In the following, the effects of the bulk Reynolds number, the particle size, the particle volume fraction and the particle–fluid density ratio on the TKE and the critical particle Reynolds number are examined. We consider two bulk Reynolds numbers $Re_b = 5746$ and 12 000, four particle sizes $a/H = 0.05, 0.75, 0.1$ and 0.15, two particle volume fractions $\Phi_0 = 0.84\%$ and 2.36%, and three density ratios 2, 10 and 100, to inspect the effects of the specific parameter, while keeping the other parameters constant, as shown in table 2. The maximum density ratio is 100, because at this density ratio the particle inertia is already considerably strong for the particle size $a/H = 0.1$ (Yu *et al.* 2017). In addition, to investigate the effect of the particle size at the same particle number density, the case of $a/H = 0.05$ and $\Phi_0 = 0.3\%$ (group 7) is added for comparison to the case of $a/H = 0.1$ and $\Phi_0 = 2.36\%$ (Group 1) at the same particle number of 360 in the channel cell.

Figure 11 shows the relative changes of the mean turbulence intensity $\widetilde{CT}$ in the entire channel and the turbulence intensity CT at the channel centre as a function of Re_p. When the other parameters are kept constant, both critical particle Reynolds numbers increase with increasing particle size a/H, bulk Reynolds number Re_b and particle–fluid density ratio ρ_r. Although both critical particle Reynolds numbers generally increase with decreasing particle volume fraction Φ_0, the dependence of the critical Re_p on the particle volume fraction for the turbulence intensity at the channel centre is more pronounced than for the total turbulence intensity in the channel. From figure 11(*a*), the critical Re_p for the total turbulence intensity is relatively insensitive to the particle volume fraction: its value for $\Phi_0 = 0.84\%$ is slightly larger than that for $\Phi_0 = 2.36\%$ at $a/H = 0.1$, and almost the same for $\Phi_0 = 0.3\%$ and $\Phi_0 = 2.36\%$ at $a/H = 0.05$. Nevertheless, the effect of
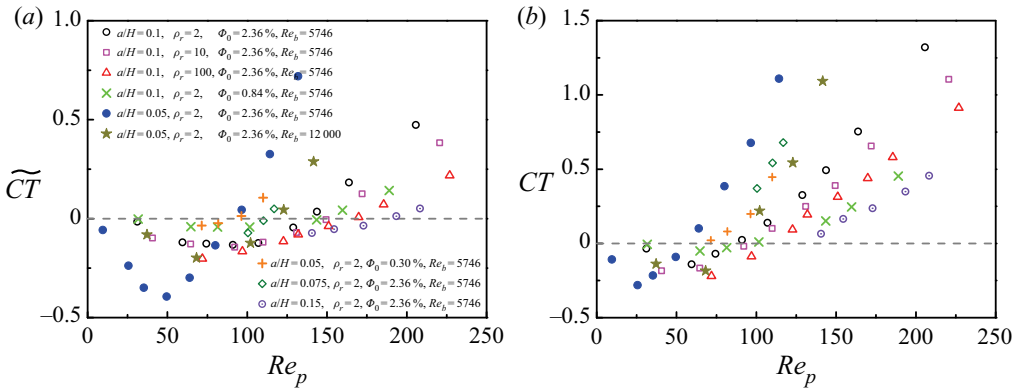
Figure 11. The relative change in (*a*) the mean turbulent intensity $\widetilde{CT}$ and (*b*) the local turbulent intensity at the channel centre CT as a function of Re_p.
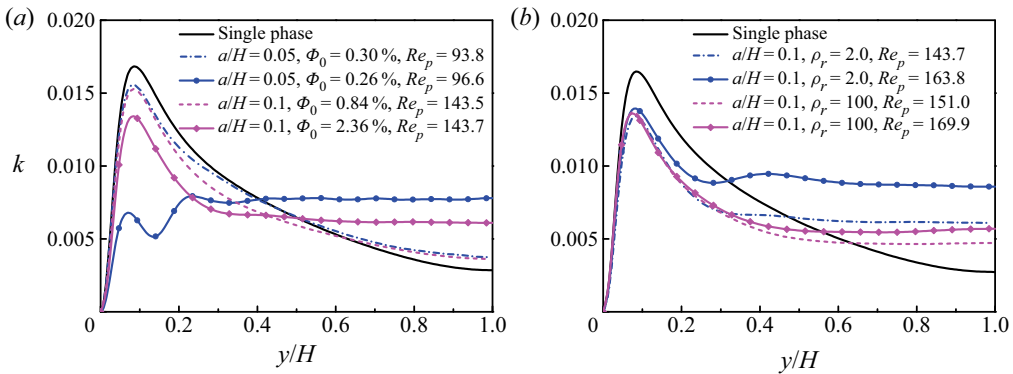

Figure 12. The TKE profiles of single-phase and particle-laden turbulent channel flows for (*a*) different particle volume fractions and (*b*) different particle–fluid density ratios.

the particle volume fraction on the TKE is significant: a higher particle volume fraction causes more enhancement in the augmentation regime or more reduction in the attenuation regime. In other words, the magnitude of the turbulence enhancement or attenuation increases with increasing particle volume fraction.

At a critical particle Reynolds number for the total TKE in the channel, the TKE is enhanced in the bulk region and attenuated in the near-wall region. Figure 12(*a*) compares the TKE profiles for different particle volume fractions at comparable Re_p near the critical value. One can see that the increase in the particle volume fraction leads to turbulence enhancement in the bulk region, but it leads to turbulence attenuation in the near-wall region. The amounts of TKE enhancement and attenuation are comparable. Therefore, the total TKE is not sensitive to the variation of the particle volume fraction near the critical state, resulting in the critical Re_p for the total TKE being insensitive to the particle volume fraction. Since the increase in the particle volume fraction leads to the increase in the TKE at the channel centre near the critical state, the critical Re_p for the turbulence augmentation at the channel centre decreases with increasing particle volume fraction.

It can be observed in figure 12(*b*) that, at comparable values of Re_p, the flow laden with particles with a larger density (or inertia) has a lower turbulence intensity in the bulk
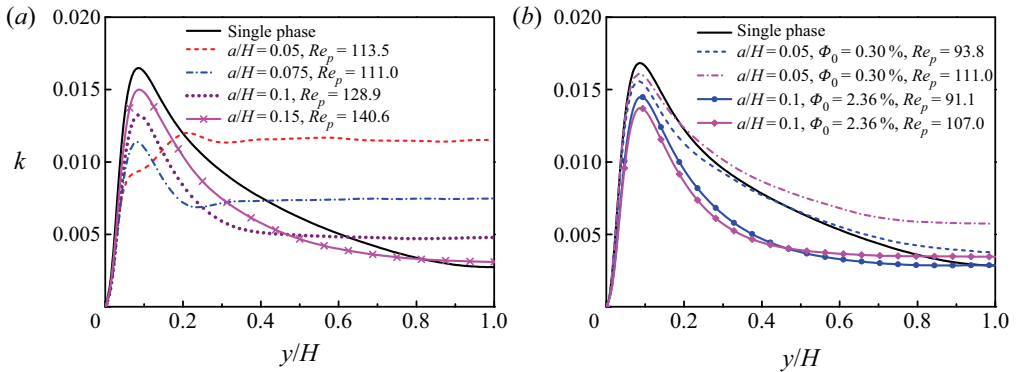
Figure 13. The TKE profiles of single-phase and particle-laden turbulent channel flows for different particle sizes at (*a*) the same particle volume fraction of 2.36 % and (*b*) the same particle number of $N_p = 360$.

region, which is responsible for the larger critical particle Reynolds number at a larger density ratio.

Figure 11 indicates that the effect of the particle size on the critical particle Reynolds number is most pronounced, compared to those of the other parameters. Some TKE profiles for different particle sizes at the same volume fraction of $\Phi_0 = 2.36$ % are shown in figure 13(*a*). The TKE in the bulk region decreases significantly with increasing particle size at comparable Re_p. Some TKE profiles at the same particle number density (360 particles in the channel domain) for $a/H = 0.05$ and $a/H = 0.1$ are depicted in figure 13(*b*). One can see that the TKEs for $a/H = 0.05$ and $\Phi_0 = 0.3$ % are still larger than those for $a/H = 0.1$ and $\Phi_0 = 2.36$ % at comparable Re_p. We will explain this particle size effect later.

The TKE profiles of single-phase and particle-laden turbulent channel flows for $Re_b = 5746$ and 12 000 at $a/H = 0.05$ and $\Phi_0 = 2.36$ % are compared in figure 14. For $Re_b = 5746$, the TKE of the particle-laden flow in the near-wall region is considerably attenuated and the large-scale vortices existing in the single-phase flow are completely suppressed at $Re_p = 64$ (i.e. $u_i/u_b = 0.3$) (see figure 10), and there is appreciable TKE augmentation in the bulk region at $Re_p = 96.6$. By contrast, for $Re_b = 12\,000$, the TKE of the particle-laden flow in the near-wall region is close to that of the single-phase flow and TKE enhancement takes place only near the channel centre at $Re_p = 102.1$. This difference indicates that stronger particle wakes (or drag force) are needed to prevail over the large-scale vortices and result in the turbulence augmentation for a higher channel (or bulk) Reynolds number. This is understandable, considering that the large-scale vortices are stronger (despite being smaller in size) at a higher channel Reynolds number. The direct effect of the particle wakes on the TKE should be related to the particle-induced TKE production rate, and we will show that the particle-induced TKE production rate normalized with the bulk velocity decreases significantly with increasing Re_b at the same particle Reynolds number from (4.14). Our effect of Re_b is consistent with the experimental results of Mena & Curtis (2020) on an upward pipe flow, who observed the change from augmentation in the total TKE at $Re_b = 2 \times 10^5$ to attenuation at $Re_b = 3.5 \times 10^5$.

4.2.2. *Criterion for turbulence modulation*

Based on our simulation data in figure 11, we propose a new criterion to distinguish between turbulence augmentation and attenuation in terms of the total TKE and the TKE
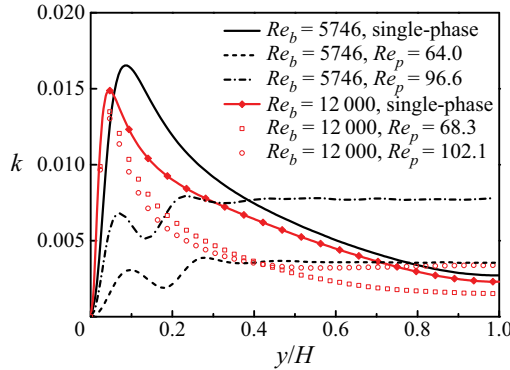
Figure 14. The TKE profiles of single-phase and particle-laden turbulent channel flows for different bulk Reynolds numbers at $a/H = 0.05$ and $\Phi_0 = 2.36\%$.
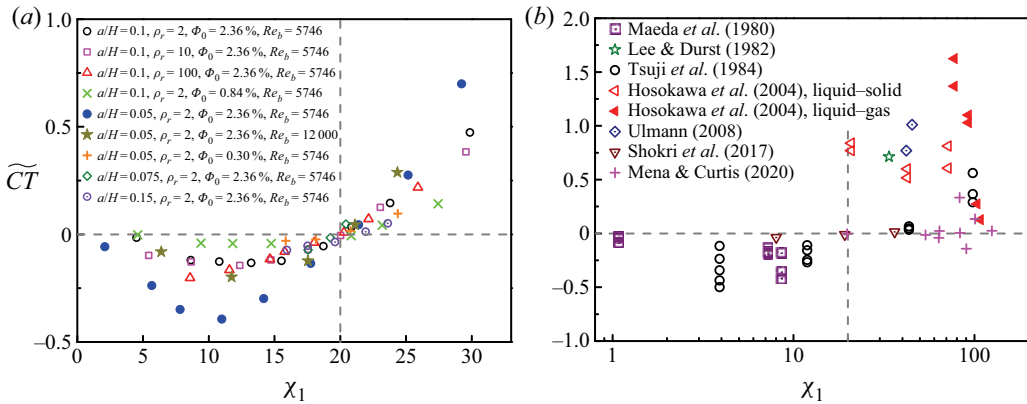

Figure 15. Relative changes of the mean turbulence intensity in the channel $\widetilde{CT}$ as a function of χ_1 for (a) the present numerical simulations and (b) previous experimental and numerical data.

at the channel centre, respectively. The parameter for the total TKE is

$$\chi_1 = \frac{Re_p}{Re_b^{0.33}(d_p/H)^{0.61}\rho_r^{0.05}}. \tag{4.3}$$

We have shown that the particle volume fraction has little effect on the critical Reynolds number for the total TKE, hence it is not included in the new parameter χ_1. The relative change of the mean turbulence intensity $\widetilde{CT}$ as a function of χ_1 is depicted in figure 15(a). It is observed that the attenuation of the total TKE occurs at $\chi_1 < 20$, and the augmentation takes place at $\chi_1 > 20$. We collect experimental data on upward pipe flows in the literature and the numerical data of Uhlmann (2008) on upward channel flow, as summarized in table 5, and compare them with our criterion of $\chi_1 = 20$ in figure 15(b). One can see that our criterion agrees well with the experimental data and the numerical data of Uhlmann (2008). There is some discrepancy between our criterion and the recent experiment of Mena & Curtis (2020). At the moment, the reason is not clear. The pipe Reynolds number of Mena & Curtis (2020) ranges from $Re_b = 2 \times 10^5$ to $Re_b = 3.5 \times 10^5$, and is much higher than ours. Further studies on the particle–turbulence interactions at high bulk Reynolds numbers are needed.

Z. Yu, Y. Xia, Y. Guo and J. Lin

Reference	Carrier	Particles	Re_b	Re_p	d_p/D	ρ_r	Φ_0
Serizawa, Kataoka & Michiyoshi (1975)	Water	Air	26 000	370	0.018	0.001	8.5×10^{-5} to 8×10^{-4}
Lee & Durst (1982)	Air	Glass	16 000	170	0.019	2080	0.0012
Maeda, Hishida & Furutani (1980)	Air	Glass, copper	20 000	1–11	0.0008–0.0024	2000–7500	6×10^{-5} to 3×10^{-4}
Tsuji *et al.* (1984)	Air	Polystyrene	23 000	10–1800	0.008–0.09	850	6.4×10^{-4} to 8×10^{-3}
Theofanous & Sullivan (1982)	Water	Air	20 000	420	0.07	0.001	0.03–0.18
Hosokawa & Tomiyama (2004)	Water	Air, ceramic	15 000, 23 000	100–1200	0.033, 0.16	0.001, 3.26	0.007–0.03
Shokri *et al.* (2017)	Water	Glass	320 000	60–600	0.01–0.04	6	0.001–0.008
Mena & Curtis (2020)	Water	Glass	200 000, 350 000	7–2848	0.0065–0.065	2.5	0.007–0.02
Uhlmann (2008)	Water	Solid particles	5400	136	0.05	2.21, 10	0.0042

Table 5. Summary of the previous experiments on upward pipe flow and the simulation of Uhlmann (2008) on upward channel flow. Here D is the diameter of the pipe and D equals $2H$ for the channel flow.
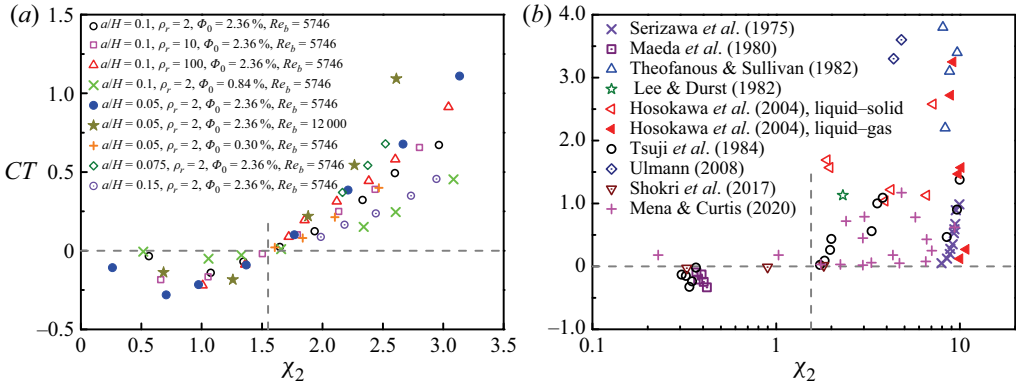
Figure 16. Relative changes of the turbulence intensity at the channel centre CT as a function of χ_2 for (*a*) the present numerical simulations and (*b*) previous experimental and numerical data.

The parameter of the criterion for the turbulence intensity at the channel centre is

$$\chi_2 = \frac{\Phi_0^{0.1}}{Re_b^{0.53}(d_p/H)^{0.61}\rho_r^{0.065}}Re_p. \tag{4.4}$$

Figure 16(*a*) shows that a value of χ_2 of approximately 1.55 can classify the turbulence augmentation and attenuation in our simulations. From figure 16(*b*), our criterion of $\chi_2 = 1.55$ for the turbulence intensity at the channel centre also agrees well with the previous experiments.

4.3. *TKE budget and modelling of interfacial term*

In this subsection, we perform a TKE budget analysis for further investigation of the effects of particles on the turbulence modulation. We also provide a preliminary modification on the model for the interfacial term in the TKE equation.

4.3.1. *Turbulent kinetic energy budget*

The volume-averaged fluid TKE equation for particle-laden flows can be derived as (Crowe *et al.* 2011; Ma *et al.* 2017; Vreman & Kuerten 2018; Peng *et al.* 2019)

$$\frac{\partial(\Phi\rho k)}{\partial t} + \frac{\partial(\Phi\rho\langle u_j\rangle k)}{\partial x_j}$$

$$= \underbrace{-\Phi\rho\langle u_i'u_j'\rangle\frac{\partial\langle u_i\rangle}{\partial x_j}}_{\mathcal{P}} \underbrace{-\Phi\left\langle\tau_{ij}'\frac{\partial u_i'}{\partial x_j}\right\rangle}_{\epsilon}$$

$$-\frac{\partial\left(\Phi\rho\left\langle u'_j\frac{u'_iu'_i}{2}\right\rangle\right)}{\partial x_j} - \underbrace{\frac{\partial(\Phi\langle u'_jp'\rangle)}{\partial x_j} + \frac{\partial(\Phi\langle u'_i\tau'_{ij}\rangle)}{\partial x_j}}_{\mathcal{D}}$$

$$+ \underbrace{\Phi(-\langle p\rangle\delta_{ij} + \langle\tau_{ij}\rangle)\left(\frac{\partial\langle u_i\rangle}{\partial x_i} - \left\langle\frac{\partial u_i}{\partial x_j}\right\rangle\right)}_{\mathcal{I}1}$$

$$\underbrace{-\frac{1}{V}\int_{S_I} n_ju_i(-p\delta_{ij} + \tau_{ij})\,\mathrm{d}s + \frac{\langle u_i\rangle}{V}\int_{S_I}(-p\delta_{ij} + \tau_{ij})n_j\,\mathrm{d}s}_{\mathcal{I}2}. \quad (4.5)$$

Here, Φ, ρ and τ_{ij} represent the fluid volume fraction, density and viscous stress, respectively. For convenience, the subscript 'f' denoting the fluid phase is omitted. The subscripts i and j denote the coordinate component, V represents the volume for averaging, S_I is the interface between the fluid and solid inside the volume V, and n is the unit vector on the particle surface pointing to the fluid. The prime in (4.5) and other places below indicates the fluctuating part of the quantity.

For the channel flow at the statistically steady state, the statistics are homogeneous in the streamwise and spanwise directions and do not change with time. Thus the derivative is only non-zero in the wall-normal (i.e. y) direction, and the averaging volume V is a thin band stretching over the streamwise and spanwise directions. In (4.5), $\mathcal{P}$ and ϵ represent the production due to the shear flow and the viscous dissipation of TKE; $\mathcal{D}$ denotes the diffusion terms including the turbulent and viscous diffusion terms. The terms $\mathcal{P}$, ϵ and $\mathcal{D}$ exist in the single-phase flow. The terms $\mathcal{I}1$ and $\mathcal{I}2$ exist only for the multiphase flows due to the presence of the interface between the two phases, and thus are called the interfacial terms or the particle source terms in the TKE equation (Crowe *et al.* 2011; Ma *et al.* 2017). We will show that the interfacial term can be approximated with two terms: the product of the mean inter-phase drag force and the mean slip velocity, and the correlation between the particle fluctuating velocity and the drag force on the particle.

Let σ_{ij} denote the total stress $\sigma_{ij} = -p\delta_{ij} + \tau_{ij}$. From the spatial averaging theorem (Crowe *et al.* 2011), one can derive

$$\Phi\left\langle\frac{\partial u_i}{\partial x_j}\right\rangle = \frac{\partial(\Phi\langle u_i\rangle)}{\partial x_j} - \frac{1}{V}\int_{S_I} n_ju_i\,\mathrm{d}s$$

$$= \Phi\frac{\partial\langle u_i\rangle}{\partial x_j} + \frac{1}{V}\int_{S_I} n_j\langle u_i\rangle\,\mathrm{d}s - \frac{1}{V}\int_{S_I} n_ju_i\,\mathrm{d}s$$

$$= \Phi\frac{\partial\langle u_i\rangle}{\partial x_j} - \frac{1}{V}\int_{S_I} n_ju'_i\,\mathrm{d}s. \quad (4.6)$$

Then, the interfacial term $\mathcal{I}1$ can be written as

$$\mathcal{I}1 = \Phi(-\langle p\rangle\delta_{ij} + \langle\tau_{ij}\rangle)\left(\frac{\partial\langle u_i\rangle}{\partial x_i} - \left\langle\frac{\partial u_i}{\partial x_j}\right\rangle\right) = \frac{1}{V}\int_{S_I}\langle\sigma_{ij}\rangle n_ju'_i\,\mathrm{d}s. \quad (4.7)$$

The interfacial term $\mathcal{I}2$ can be written as

$$\mathcal{I}2 = -\frac{1}{V}\int_{S_I}\sigma_{ij}n_ju'_i\,\mathrm{d}s. \quad (4.8)$$

Thus, the total interfacial term has the form (Ma *et al.* 2017; Vreman & Kuerten 2018)

$$\mathcal{I} = \mathcal{I}1 + \mathcal{I}2 = -\frac{1}{V} \int_{S_I} \sigma'_{ij} n_j u'_i \, \mathrm{d}s. \tag{4.9}$$

Accurate computation of the interfacial term via the integration of the stress on the particle surface is difficult for the fictitious domain method, and here we obtain it from the TKE equation at the statistically steady state: $\mathcal{I} = -(\mathcal{P} + \epsilon + \mathcal{D})$. Since the terms $\mathcal{P}$, ϵ and $\mathcal{D}$ are computed by averaging over time, and over the streamwise and spanwise directions (not over the wall-normal direction), the averaging volume can be regarded as a very thin band containing the plane $y = y_i$, where $y = y_i$ is the y coordinate of the computational grid.

The profiles of the production, dissipation, diffusion and interfacial terms in the TKE equation for the case of $a/H = 0.05$, $\Phi_0 = 2.36\,\%$, $\rho_r = 2.0$ and $Re_b = 5746$ are depicted in figure 17. Similar to the behaviour of the Reynolds stress and the r.m.s. velocities in figure 7, the production rate of TKE $\mathcal{P}$ first decreases and then increases, as u_i/u_b increases; $\mathcal{P}$ is attenuated by the particles for $u_i/u_b \leq 0.45$, similar to the Reynolds stress in figure 7(*b*). In the bulk region, the particle wakes do not contribute significantly to the Reynolds stress and $\mathcal{P}$, since the mean fluid velocity there is nearly uniform at a high u_i/u_b. The reduction in $\mathcal{P}$ is clearly caused by the suppression of the large-scale vortices. For the present particle-laden flow where there is a mean interphase slip velocity, the interfacial term is always larger than zero and increases with increasing u_i/u_b, as shown in figure 17(*c*). Hence, the interfacial term can be regarded as the particle-induced TKE production. At a high u_i/u_b, the strong particle wakes cause a large TKE and accordingly a large viscous dissipation ϵ. The large drag force at a high u_i/u_b also leads to a large interfacial term $\mathcal{I}$. In the bulk region, the shear-induced production $\mathcal{P}$ and the diffusion $\mathcal{D}$ are small; therefore, the dissipation ϵ is nearly equal to the particle-induced production $\mathcal{I}$ in magnitude.

The production, dissipation and interfacial terms for different particle sizes at the same particle number density and comparable particle Reynolds numbers are compared in figure 18(*a*). It has been shown in figure 13(*b*) that smaller particles can cause more augmentation in the TKE at the same particle number density and comparable particle Reynolds numbers. Figure 18(*a*) shows the same behaviour for the interfacial and dissipation terms: they are larger for smaller particles at the same particle number density and Reynolds number. It should be noted that the interfacial term is larger for smaller particles ($a/H = 0.05$) in the bulk region even if the local particle number density there is significantly smaller for smaller particles (because the particle concentration is higher in the near-wall region for smaller particles), as shown in figure 19. Figure 18(*b*) compares the production, dissipation and interfacial terms for $\rho_r = 2$ and 100 at $a/H = 0.1$. Overall, the interfacial term is greater for the less dense particles with lower inertia. The reason should be related to the particle concentration distribution. For $\rho_r = 2$ ($Re_p = 163.8$, $a/H = 0.1$), there is a peak at around $y = 0.4H$ mainly as a result of the Saffman effect, which drives the particles away from the wall, whereas for $\rho_r = 100$, the particle concentration distribution is more homogeneous across the channel. The higher particle concentration at around $y = 0.4H$ for $\rho_r = 2$ ($a/H = 0.1$) in figure 19 should be responsible for its larger interfacial term at around $y = 0.4H$ in figure 18(*b*).

The reason for the general decrease in the critical Reynolds number (particularly the one for the TKE at the channel centre) with decreasing particle size and density ratio and with increasing particle volume fraction should be related to the larger interfacial term (i.e. particle-induced TKE production) for a smaller particle size or density ratio, or a larger particle volume fraction at the same particle Reynolds number. However, it should be
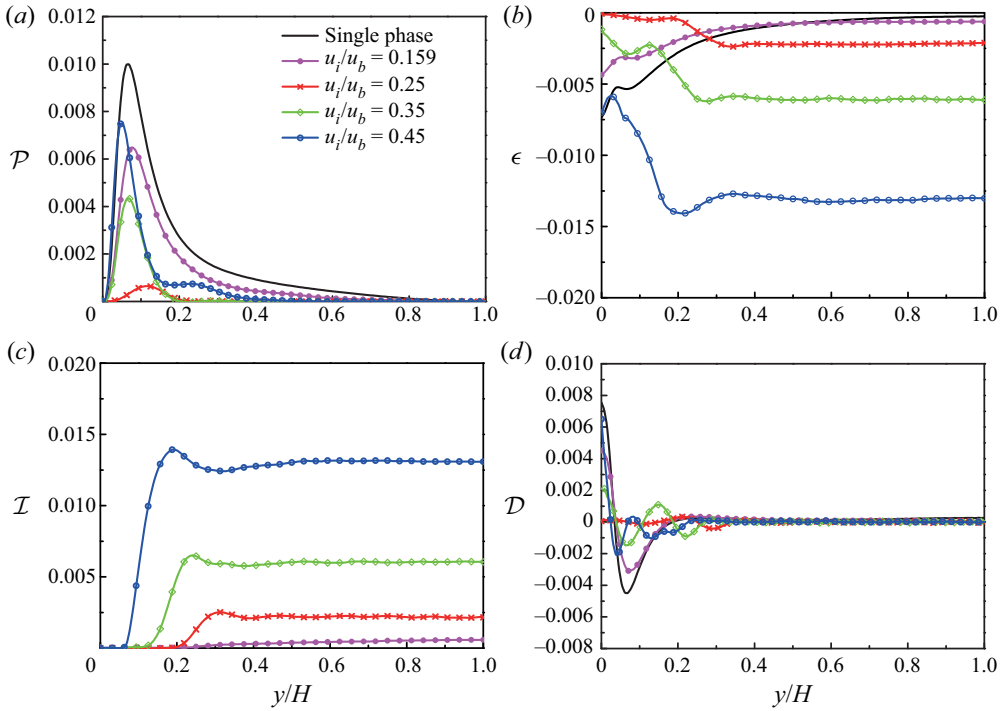
Figure 17. Profiles of the terms in the TKE equation for the typical case of $a/H = 0.05$, $\Phi_0 = 2.36\%$ and $Re_b = 5746$: (*a*) the production term $\mathcal{P}$, (*b*) the dissipation term ϵ, (*c*) the interfacial term $\mathcal{I}$ and (*d*) the diffusion term $\mathcal{D}$. All terms are normalized with $\rho_f u_b^3/H$.

Figure 18. Production, dissipation and interfacial terms in the TKE equation, normalized with $\rho_f u_b^3/H$, for (*a*) different particle sizes a/H at the same particle number density and (*b*) different particle–fluid density ratios ρ_r.

913 A3-28

Figure 19. Profiles of the particle volume fraction for different particle sizes at the same particle number density and different particle–fluid density ratios.

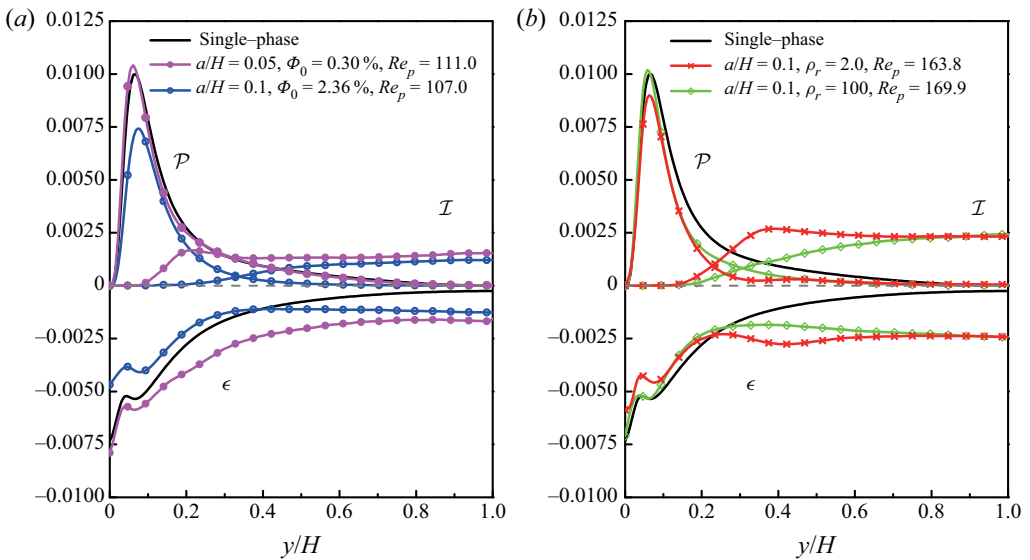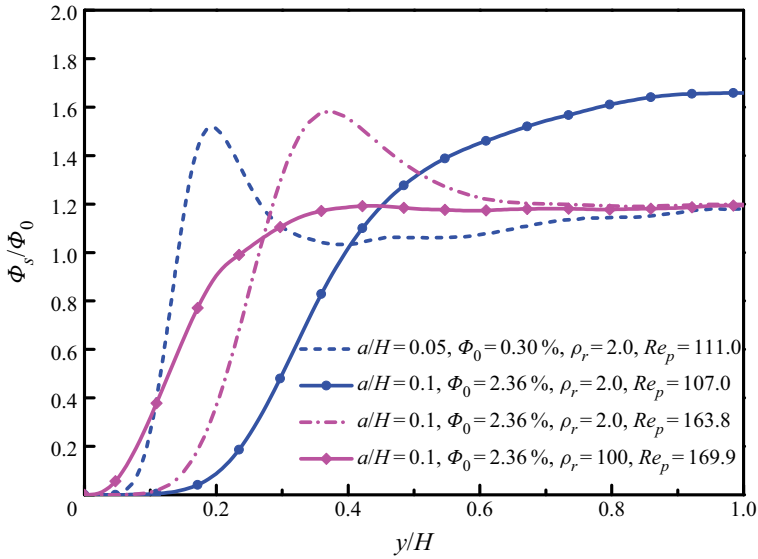noted that, although the interfacial term $\mathcal{I}$ or the dissipation rate ϵ is generally correlated with the TKE, a higher $\mathcal{I}$ or ϵ does not always mean a higher TKE. For example, the TKE at the channel centre for $\rho_r = 2$ and $Re_p = 163.8$ is higher than that for $\rho_r = 100$ and $Re_p = 169.9$, as shown in figure 12(*b*), but $\mathcal{I}$ and ϵ at the channel centre are almost the same for the two cases, as shown in 18(*b*). Hence, the dependence of the interfacial term on the parameters can be regarded as the main reason for the dependence of the critical particle Reynolds number on the corresponding parameters, but it is not the only reason. As for the effect of the density ratio, another reason may be that less dense particles have stronger hydrodynamic interactions and consequently may have larger variations in the instantaneous slip velocity at the channel centre where the flow is dominated by the particle wakes, when the mean interphase slip velocity is the same.

4.3.2. *Analysis of the interfacial term in the dilute limit*

We here attempt to provide an explanation for the effects of the particle size and the bulk Reynolds number on the TKE at the same particle Reynolds number by simplifying the interfacial term in the dilute limit. The interfacial term $\mathcal{I}1$ is not important, since the average of the velocity gradient should be close to the gradient of the average velocity, as shown in the calculation of Peng *et al.* (2019). Following the analysis of Crowe *et al.* (2011), we neglect the effects of the particle rotation. We further assume that all particle surfaces are inside the volume V, which is reasonable for a homogeneous system such as particle sedimentation in the bulk region. The fluid velocity on the surface for a non-rotating particle k is equal to the particle translational velocity, which is a constant for the integration on the particle surface. Then, the interfacial term $\mathcal{I}2$ can be simplified as

$$-\frac{1}{V}\int_{S_I} u_i(-p\delta_{ij} + \tau_{ij})\,\mathrm{d}s + \frac{\langle u_i \rangle}{V}\int_{S_I}(-p\delta_{ij} + \tau_{ij})n_j\,\mathrm{d}s = \frac{1}{V}\sum_k (\langle u_i \rangle - u_{pki})F_{ki}, \quad (4.10)$$

where F_{ki} is the drag force on the particle k and u_{pki} is the translational velocity of the particle k.

For vertical channel flow, the drag force is mainly directed in the streamwise direction and thus we neglect the contributions from the other two directions:

$$\frac{1}{V} \sum_k (\langle u_i \rangle - u_{pki}) F_{ki} \approx \frac{1}{V} \sum_k (\langle u_f \rangle - u_{pk}) F_k, \tag{4.11}$$

where u_f, u_{pk} and F_k represent the fluid velocity, the particle translational velocity and the drag force on the particle k in the streamwise direction, respectively. Considering that $\langle u_f \rangle - u_{pk} = \langle u_f \rangle - \langle u_p \rangle - u'_{pk}$ (with u'_{pk} being the particle velocity fluctuation), we have

$$\mathcal{I} \approx \frac{1}{V} \sum_k (\langle u_f \rangle - \langle u_p \rangle - u'_{pk}) F_k = (\langle u_f \rangle - \langle u_p \rangle) \frac{1}{V} \sum_k F_k - \frac{1}{V} \sum_k u'_{pk} F_k. \tag{4.12}$$

The first term on the right-hand side is the product of the mean inter-phase drag force and the mean slip velocity, and was regarded as the main contribution to the interfacial term (Troshko & Hassan 2001; Crowe *et al.* 2011).

For particle-laden flows in the dilute limit, one may assume that each particle settles with the same slip velocity $u_r = \langle u_f \rangle - \langle u_p \rangle$, and then

$$(\langle u_f \rangle - \langle u_p \rangle) \frac{1}{V} \sum_k F_k = n \frac{u_r^3 C_D \pi a^2 \rho_f}{2} = n \frac{Re_p^3 \nu^3 C_D \pi \rho_f}{16a}, \tag{4.13}$$

in which $n = \Phi_s/(4\pi a^3/3)$ is the particle number density and C_D is the standard drag coefficient. The interfacial term in our simulations is normalized with $\rho_f u_b^3/H$. From (4.13), one has

$$\frac{(\langle u_f \rangle - \langle u_p \rangle) \frac{1}{V} \sum_k F_k}{\rho_f u_b^3/H} \sim n^* \frac{Re_p^3 C_D}{Re_b^3(a/H)} \sim \Phi_s \frac{Re_p^3 C_D}{Re_b^3(a/H)^4}, \tag{4.14}$$

where n^* denotes the dimensionless particle number density. The drag coefficient C_D is a function of the particle Reynolds number alone.

Hence, the above dimensionless interfacial term is inversely proportional to the particle size at the same particle number density n, Re_p and Re_b, which provides an explanation for the early observations that the interface term is larger for smaller particles at the same particle Reynolds number and particle number density in figure 18(a) and the critical particle Reynolds number increases significantly with increasing particle size in figure 11. Equation (4.14) also explains why the dimensionless TKE in the bulk region is significantly smaller for a higher bulk Reynolds number at comparable particle Reynolds numbers in figure 14 and why the critical particle Reynolds number is higher at a higher bulk Reynolds number in figure 11.

4.3.3. *Modelling of the interfacial term*

Modelling of the interfacial term is crucial for the Reynolds-averaged Navier–Stokes (RANS) model and the Reynolds stress model (i.e. second-order moment model) for the simulations of industrial-scale multiphase turbulent flows (Ansys 2013;

Ma *et al.* 2017, 2020). The Troshko–Hassan model (Troshko & Hassan 2001) is one of the widely used models for the interfacial term:

$$\mathcal{I} = C_n \bar{F} u_r, \tag{4.15}$$

where $\bar{F}$ is the volume-averaged drag force, $\bar{F} = (1/V) \sum_k F_k$, and C_n is a coefficient. In the Ansys FLUENT software, a value of 0.75 is recommended for C_n (Ansys 2013). Ma *et al.* (2017) determined C_n as a function of Re_p, from the interface-resolved DNS data of Santarelli, Roussel & Fröhlich (2016) on the bubbly flow in a vertical channel:

$$C_n = 0.18 Re_p^{0.23}. \tag{4.16}$$

In the following, we attempt to evaluate C_n from our DNS data. Following Ma *et al.* (2017), the drag force is determined directly from the simulations, rather than from the drag model. For the channel flow at the statistically stationary state, the fluid mean momentum equation in the streamwise direction can be written as follows (Yu *et al.* 2017):

$$\frac{\mathrm{d}}{\mathrm{d}y}\left(\Phi_f \mu \frac{\mathrm{d}\langle u_f \rangle}{\mathrm{d}y}\right) + \Phi_f\left(-\frac{\mathrm{d}p_e}{\mathrm{d}x}\right) + \frac{\mathrm{d}}{\mathrm{d}y}(\Phi_f \rho_f \langle -u'_f v'_f \rangle) - \bar{F} = 0. \tag{4.17}$$

For upward flow, one can compute the pressure gradient from the force balance,

$$-\mathrm{d}p_e/\mathrm{d}x = \tau_w/H + \Phi_0(\rho_s - \rho_f)g, \tag{4.18}$$

where τ_w is the mean shear stress on the sidewalls. Then, the volume-averaged drag force can be calculated from (4.17). The calculation of the drag force at the channel centre can be simplified, if the flow is homogeneous there (i.e. $\mathrm{d}(\cdot)/\mathrm{d}y = 0$). The solid-phase mean momentum equation in the streamwise direction is (Yu *et al.* 2017)

$$\frac{\mathrm{d}}{\mathrm{d}y}(\Phi_s \langle \sigma_s \rangle_{xy}) + \Phi_s\left(-\frac{\mathrm{d}p_e}{\mathrm{d}x}\right) - \Phi_s(\rho_s - \rho_f)g + \frac{\mathrm{d}}{\mathrm{d}y}(\Phi_s \rho_s \langle -u'_s v'_s \rangle) + \bar{F} = 0. \tag{4.19}$$

For a homogeneous flow, the fluid momentum equation (4.17) reduces to $\bar{F} = \Phi_f(-\mathrm{d}p_e/\mathrm{d}x)$, and the solid-phase momentum equation (4.19) reduces to $\bar{F} = \Phi_s(\rho_s - \rho_f)g - \Phi_s(-\mathrm{d}p_e/\mathrm{d}x)$. From these two equations, one can obtain the pressure gradient and the drag force as

$$\bar{F} = \Phi_f\left(-\frac{\mathrm{d}p_e}{\mathrm{d}x}\right) = \Phi_f \Phi_s(\rho_s - \rho_f)g, \tag{4.20}$$

which was used by Ma *et al.* (2017) for the calculation of the drag force. Equation (4.17) is used in the present study, because, for $\rho_r = 100$, the gradient of the particle Reynolds stress at the channel centre in (4.19) is found to be not negligibly small. For $\rho_r = 2$, the results obtained with the two methods are close to each other for relatively high particle Reynolds numbers.

The mean C_n values for the channel centre region $-0.1 \leq y/H \leq 0.1$ (here $y = 0$ corresponding to the channel centre) as a function of Re_p for different particle sizes, different volume fractions and different density ratios are plotted in figure 20(*a*). When we ran the cases for the study of the criterion on the TKE augmentation and attenuation, the data for the TKE budget were not computed. Owing to our limited computer resources, only some cases were selected for the generation of the data for the modelling of the interfacial term. Figure 20(*a*) shows that the coefficient C_n decreases with increasing particle Reynolds number for the same group of control parameters, and is higher for
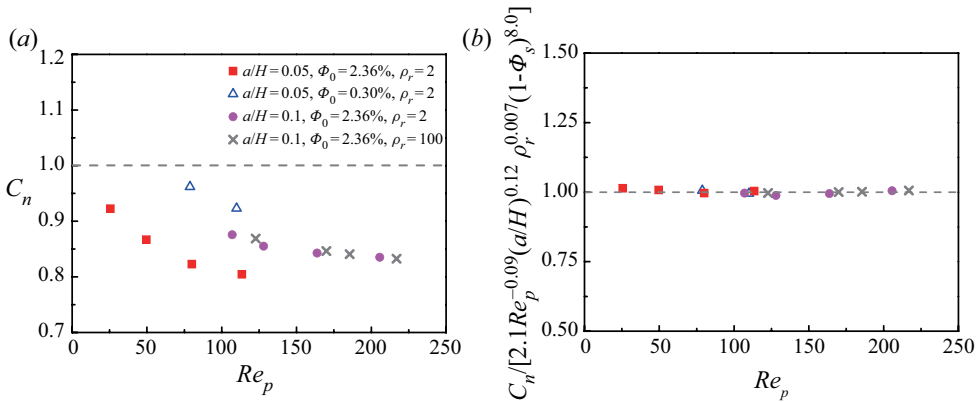
Figure 20. Plots of (*a*) C_n versus Re_p for different particle sizes, particle volume fractions and density ratios, and (*b*) $C_n = 2.1 Re_p^{-0.09} (a/H)^{0.12} \rho_r^{0.007} (1 - \Phi_s)^{8.0}$ as a function of Re_p.

a lower particle volume fraction or a larger particle size at the same particle Reynolds number. The effect of the density ratio is small. The fitting of our data yields

$$C_n = 2.1 Re_p^{-0.09} \left(\frac{a}{H} \right)^{0.12} \rho_r^{0.007} (1 - \Phi_s)^{8.0}. \tag{4.21}$$

Figure 20(*b*) shows that the above model of C_n fits our data well.

The dependence of our C_n on Re_p appears to be inconsistent with that of Ma *et al.* (2017). Our C_n (4.21) decreases with increasing Re_p, whereas theirs (4.16) increases with increasing Re_p. However, our dependence of C_n on Re_p is examined at the same particle size and particle volume fraction, whereas theirs is examined at different particle sizes and particle volume fractions. Their results are consistent with ours in that C_n is larger for larger particles and a lower particle volume fraction. Thus, we suspect that the dependence of their C_n on Re_p is caused by the effects of the particle size and the particle volume fraction, rather than Re_p. In addition, we note that they used the data on bubbly flow at $Re_p > 230$, whereas we consider solid particles at $Re_p < 230$.

The reasons for the dependence of C_n on the particle Reynolds number, the particle size, the particle volume fraction and the density ratio are not clear, but should be related to the effects of the second term on the right-hand side in (4.12), i.e. the particle velocity fluctuation term: $(1/V) \sum_k u'_{pk} F_k$. If the effect of the particle rotation is not important and (4.12) is a good approximation to the interfacial term, then $C_n \approx 1 - (1/V) \sum_k u'_{pk} F_k / (u_r \bar{F})$. Particles may be accelerated by the particle wakes, resulting in the positive correlation between the particle fluctuating velocity and the force on the particle. An increase in the particle Reynolds number or the particle volume fraction, or a decrease in the particle size or the density ratio, may cause a larger particle velocity fluctuation and the increase in $(1/V) \sum_k u'_{pk} F_k / (u_r \bar{F})$, i.e. the decrease in C_n. A more significant effect of the density ratio on C_n than that shown in figure 20(*a*) was expected from this reasoning. In fact, if the drag force is calculated with (4.20), instead of (4.17), the difference in C_n for $\rho_r = 100$ and $\rho_r = 2$ would be more pronounced. Using (4.17), C_n can be determined from:

$$\frac{\mathcal{I}}{\rho_f u_b^3 / H} = \frac{C_n \Phi_f \Phi_s (\rho_s - \rho_f) g u_r H}{\rho_f u_b^3} = C_n \Phi_f \Phi_s \frac{3}{8(a/H)} \left(\frac{u_i}{u_b} \right)^2 \frac{u_r}{u_b}. \tag{4.22}$$

913 A3-32

Group no.	u_i/u_b	Ga	Re_τ	$-\mathrm{d}p_e/\mathrm{d}x$	Re_p	$\widetilde{CT}$	CT
Single-phase	—	—	180.8	3.93×10^{-3}	—	—	—
	—	—	345.9	3.32×10^{-3}	—	—	—
Group 1	0.1	49.8	178.6	4.75×10^{-3}	31.1	−0.016	−0.035
	0.15	74.6	175.6	5.73×10^{-3}	59.4	−0.120	−0.141
	0.175	87.1	175.8	6.46×10^{-3}	74.4	−0.126	−0.070
	0.2	99.5	175.6	7.28×10^{-3}	91.1	−0.133	0.023
	0.225	112.0	176.8	8.27×10^{-3}	107.0	−0.123	0.123
	0.25	124.4	179.2	9.42×10^{-3}	128.9	−0.055	0.322
	0.275	136.8	184.1	1.08×10^{-2}	143.7	0.035	0.493
	0.3	149.3	188.1	1.23×10^{-2}	163.8	0.182	0.753
	0.35	174.2	197.4	1.56×10^{-2}	205.7	0.473	1.320
Group 2	0.1	49.8	181.1	4.86×10^{-3}	40.6	−0.098	−0.185
	0.15	74.6	178.3	5.84×10^{-3}	64.6	−0.128	−0.167
	0.2	99.5	177.8	7.37×10^{-3}	92.2	−0.144	−0.019
	0.225	112.0	179.1	8.37×10^{-3}	110.0	−0.119	0.100
	0.25	124.4	181.0	9.50×10^{-3}	131.0	−0.070	0.249
	0.275	136.8	184.1	1.08×10^{-2}	149.5	−0.005	0.390
	0.3	149.3	187.1	1.22×10^{-2}	172.1	0.126	0.656
	0.35	174.2	194.3	1.50×10^{-2}	220.7	0.383	1.105
Group 3	0.1	49.8	178.8	4.76×10^{-3}	71.9	−0.203	−0.220
	0.15	74.6	180.0	5.92×10^{-3}	96.9	−0.166	−0.088
	0.2	99.5	183.8	7.63×10^{-3}	122.7	−0.115	0.089
	0.225	112.0	186.1	8.68×10^{-3}	132.0	−0.081	0.194
	0.25	124.4	188.3	9.82×10^{-3}	151.0	−0.039	0.313
	0.275	136.8	191.1	1.11×10^{-2}	169.9	0.009	0.443
	0.3	149.3	194.0	1.25×10^{-2}	186.5	0.072	0.581
	0.35	174.2	200.2	1.57×10^{-2}	226.9	0.218	0.912
Group 4	0.1	49.8	179.9	4.24×10^{-3}	31.6	−0.002	−0.005
	0.15	74.6	178.1	4.55×10^{-3}	64.7	−0.041	−0.051
	0.175	87.1	178.3	4.82×10^{-3}	81.4	−0.042	−0.028
	0.2	99.5	178.6	5.12×10^{-3}	101.6	−0.042	0.010
	0.25	124.4	180.0	5.90×10^{-3}	143.5	−0.006	0.152
	0.27	134.4	181.7	6.30×10^{-3}	159.7	0.042	0.246
	0.3	149.3	184.1	6.94×10^{-3}	189.0	0.143	0.454
Group 5	0.092	22.9	189.5	5.73×10^{-3}	9.5	−0.057	−0.108
	0.159	39.6	174.1	8.15×10^{-3}	25.6	−0.238	−0.281
	0.2	49.8	161.1	1.02×10^{-2}	35.3	−0.349	−0.216
	0.25	62.2	166.9	1.44×10^{-2}	49.6	−0.394	−0.092
	0.3	74.6	180.1	1.99×10^{-2}	64.0	−0.299	0.101
	0.35	87.1	195.4	2.63×10^{-2}	80.1	−0.135	0.384
	0.4	99.5	207.0	3.35×10^{-2}	96.6	0.044	0.677
	0.45	112.0	214.8	4.14×10^{-2}	113.5	0.326	1.109
	0.5	124.4	219.1	5.01×10^{-2}	131.9	0.719	1.696
	0.7	174.2	255.2	9.51×10^{-2}	209.7	1.355	2.512

Table 6. Results for the simulation cases: groups 1–5. Pressure gradients $(-\mathrm{d}p_e/\mathrm{d}x)$ are normalized by $\rho_f u_b^2/H$.

Now we compare two cases: $(a/H, \rho_r, u_i/u_b) = (0.1, 2, 0.3)$ in group 1 and $(a/H, \rho_r, u_i/u_b) = (0.1, 100, 0.25)$ in group 3. From table 6, the particle Reynolds numbers for these two cases are $Re_p = 163.8$ and $Re_p = 169.9$, respectively. From figures 18(*b*) and 19, the interfacial term and the particle volume fraction at the channel centre for

these two cases are nearly the same. The mean slip velocities are also close to each other, since the particle Reynolds numbers are close. The relative difference in C_n is around 16 %, since the settling coefficients u_i/u_b are 0.3 and 0.275, respectively. As mentioned earlier, the effect of the particle Reynolds stress or the shear flow on the drag force even at the channel centre cannot be neglected for $\rho_r = 100$ in the range of Re_p studied. When gravity is not considered, i.e. $u_i/u_b = 0$, there is still a pronounced mean drag force on the particles at the channel centre for $\rho_r = 100$ (Yu *et al.* 2017), which is mainly balanced with the gradient of the particle Reynolds stress.

Only a preliminary work on the modelling of the interfacial term in the TKE equation is conducted here. We intend to do further studies on the models for the near-wall region and lower particle Reynolds numbers in the future. The drag and lift models, the RANS model and the second-order model for particle-laden turbulent flows based on the interface-resolved DNS data are good subjects for extensive future work.

4.4. *Flow friction and total drag*

In this subsection, we will explore the effects of the particle sedimentation on the wall friction and total flow drag. The summation of the fluid momentum equation (4.17) and the solid-phase momentum equation (4.19) yields (Picano *et al.* 2015; Yu *et al.* 2017)

$$\frac{d}{dy}(\Phi_f \langle \sigma_f \rangle_{xy} + \Phi_s \langle \sigma_s \rangle_{xy}) + \left(-\frac{dp_e}{dx} \right)$$
$$+ \frac{d}{dy}(\Phi_f \rho_f \langle -u_f' v_f' \rangle + \Phi_s \rho_s \langle -u_s' v_s' \rangle) - \Phi_s(\rho_s - \rho_f)g = 0. \tag{4.23}$$

Substituting (4.18) into (4.23) yields

$$-\frac{\tau_w}{H} = \frac{d}{dy}(\Phi_f \langle \sigma_f \rangle_{xy} + \Phi_s \langle \sigma_s \rangle_{xy}) + (\Phi_0 - \Phi_s)(\rho_s - \rho_f)g$$
$$+ \frac{d}{dy}(\Phi_f \rho_f \langle -u_f' v_f' \rangle + \Phi_s \rho_s \langle -u_s' v_s' \rangle). \tag{4.24}$$

The friction coefficient is defined as $C_f = 2\tau_w/\rho_f u_b^2$. Applying triple integrations (i.e. $\int_0^1 dy \int_0^y dy \int_0^y dy$) to (4.24), one obtains (Fukagata, Iwamoto & Kasagi 2002; Zhu *et al.* 2020*a*):

$$C_f = \underbrace{\frac{6}{Re_b} \int_0^1 (1-y)\Phi_f \left(\frac{du_f^*}{dy} \right) dy}_{C_{fv}} + \underbrace{6 \int_0^1 (1-y)(\Phi_f \langle -u_f^{*'} u_f^{*'} \rangle) dy}_{C_{fR}}$$
$$+ \underbrace{6 \int_0^1 (1-y)\frac{\Phi_s}{\rho_f u_b^2} \langle \sigma_s \rangle_{xy} dy}_{C_{pI}} + \underbrace{6 \int_0^1 (1-y)(\Phi_s \rho_r \langle -u_s^{*'} u_s^{*'} \rangle) dy}_{C_{pR}}$$
$$+ \underbrace{\left(-3 \int_0^1 (1-y)^2 (\Phi_s - \Phi_0)(\rho_r - 1)Fr \, dy \right)}_{C_g}, \tag{4.25}$$
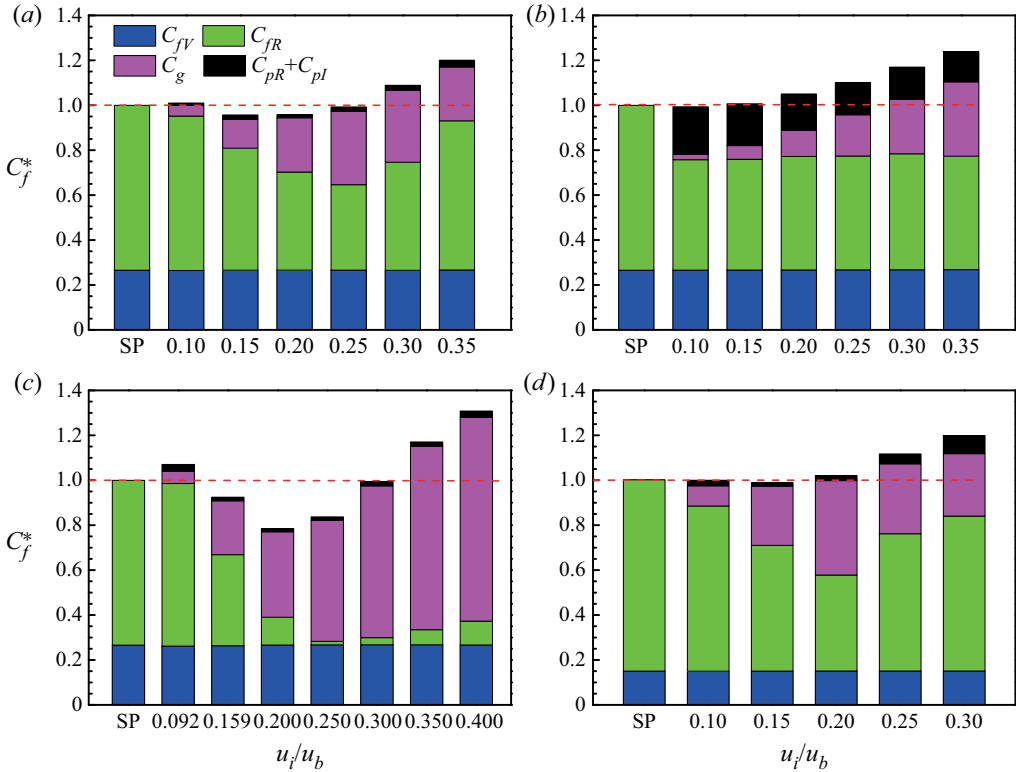
Figure 21. Contributions of the fluid viscous stress C_{fV}, the fluid Reynolds stress C_{fR}, the particle total stress $C_{pR} + C_{pI}$ and the gravity term C_g to the wall friction C_f at different u_i/u_b for: (*a*) group 1, $(a/H, \rho_r, Re_b) = (0.1, 2, 5746)$; (*b*) group 3, $(a/H, \rho_r, Re_b) = (0.1, 100, 5746)$; (*c*) group 5, $(a/H, \rho_r, Re_b) = (0.05, 2, 5746)$; and (*d*) group 6, $(a/H, \rho_r, Re_b) = (0.05, 2, 12\,000)$. The results are normalized by C_f for the single-phase case. SP denotes the single-phase case, rather than the particle-laden flow at $u_i/u_b = 0$.

where C_{fV}, C_{fR}, C_{pI}, C_{pR} and C_g are the contributions of the fluid viscous stress, the fluid Reynolds stress, the particle inner stress, the particle Reynolds stress and gravity, respectively. Here, y is the dimensionless coordinate normalized with H, with the wall position shifted to $y = 0$, and u^* and v^* denote the dimensionless velocity components normalized by u_b, and Fr represents the Froude number defined by $Fr = gH/u_b^2$. Note that the particle Reynolds stress is calculated by using the velocities at the Eulerian grids inside the particle regions rather than the particle translational velocities. To derive (4.25), the following relations are used:

$$(\Phi_f \langle \sigma_f \rangle_{xy} + \Phi_s \langle \sigma_s \rangle_{xy})|_{y=0} = \tau_w, \tag{4.26}$$

$$\int_0^1 \int_0^y f \, \mathrm{d}y \, \mathrm{d}y = \int_0^1 (1-y) f \, \mathrm{d}y, \quad \int_0^1 \int_0^y \int_0^y f \, \mathrm{d}y \, \mathrm{d}y \, \mathrm{d}y = \frac{1}{2} \int_0^1 (1-y)^2 f \, \mathrm{d}y. \tag{4.27}$$

Each contribution, normalized with the friction coefficient of the single-phase case, is plotted in figure 21 for the different settling coefficients. The single-phase results (denoted by SP) are also shown for comparison. Because the particle volume fraction is small (2.36 %), the contribution from the particle stress is small for $\rho_r = 2$. However, it is significant for $\rho_r = 100$. Another notable difference between the two density ratios

Group no.	u_i/u_b	Ga	Re_τ	$-\mathrm{d}p_e/\mathrm{d}x$	Re_p	$\widetilde{CT}$	CT
Group 6	0.1	52.0	345.7	5.09×10^{-3}	37.2	-0.081	-0.138
	0.15	77.9	343.0	7.25×10^{-3}	68.3	-0.198	-0.184
	0.2	103.9	348.9	1.05×10^{-2}	102.1	-0.123	0.219
	0.225	116.9	353.9	1.24×10^{-2}	122.9	0.044	0.543
	0.25	129.9	363.7	1.47×10^{-2}	141.6	0.288	1.092
Group 7	0.29	72.2	181.7	5.86×10^{-3}	71.5	-0.0348	0.021
	0.315	78.4	183.4	6.37×10^{-3}	78.8	-0.023	0.079
	0.36	89.6	185.4	7.14×10^{-3}	93.8	0.013	0.199
	0.4	99.5	186.9	7.88×10^{-3}	111.0	0.106	0.447
Group 8	0.28	104.5	180.7	1.30×10^{-2}	100.4	-0.072	0.371
	0.3	112.0	184.7	1.50×10^{-2}	110.1	-0.011	0.542
	0.312	116.4	186.9	1.60×10^{-2}	116.9	0.048	0.679
Group 9	0.185	138.1	177.4	5.83×10^{-3}	140.6	-0.073	0.087
	0.2	149.3	177.9	6.20×10^{-3}	154.5	-0.053	0.165
	0.215	160.5	179.7	6.64×10^{-3}	172.8	-0.035	0.237
	0.23	171.7	181.2	7.10×10^{-3}	193.4	0.012	0.349
	0.24	179.1	182.6	7.44×10^{-3}	208.3	0.051	0.456

Table 7. Results for the simulation cases: groups 6–9.

is that, as u_i/u_b increases, the contribution from the fluid Reynolds stress for $\rho_r = 2$ first decreases and then increases, whereas it is almost independent of u_i/u_b for $\rho_r = 100$. For the particle-laden flows, generally the wall friction first decreases and then increases as u_i/u_b increases. The decrease in C_f for $\rho_r = 2$ is caused by the decrease in the fluid Reynolds stress, and the subsequent increase in C_f is mainly due to the increase in the gravity term C_g for $(a/H, \rho_r, Re_b) = (0.05, 2, 5746)$ and $(a/H, \rho_r, Re_b) = (0.1, 100, 5746)$, while it is mainly due to the increase in the fluid Reynolds stress for $(a/H, \rho_r, Re_b) = (0.1, 2, 5746)$ and $(a/H, \rho_r, Re_b) = (0.05, 2, 12\,000)$. The attenuation in the fluid Reynolds stress for $(a/H, \rho_r, Re_b) = (0.05, 2, 5746)$ is most pronounced, compared to the other cases, because the particle-induced TKE production (or the effect of the particle wakes) is more significant for smaller particles or a lower bulk Reynolds number, as discussed earlier in association with (4.14). The contributions from the gravity term at relatively large settling coefficients for $(a/H, \rho_r, Re_b) = (0.05, 2, 5746)$ are also most pronounced, because the gravity term is larger for smaller particles, as implied by $(\rho_r - 1)Fr = 3(u_i/u_b)^2/(8a/H)$ from (2.25), and the particle concentration distribution is more homogeneous at a higher bulk Reynolds number, which means that Φ_s is closer to Φ_0.

Figure 21 shows that there is a reduction in the wall friction at intermediate settling coefficients, compared to the single-phase flow. However, this does not mean drag reduction, since the total flow drag is normally measured with the pressure drop at the same flow rate. The pressure gradients for all cases studied are presented in tables 6 and 7. The total flow drag increases monotonically with increasing u_i/u_b without any drag reduction.

5. Conclusion

Interface-resolved direct numerical simulations (IR-DNS) of upward turbulent channel flows laden with finite-size spherical particles have been performed, and the modulation of the turbulence intensity by heavy particles has been investigated at $Re_b = 5746$ and $12\,000$,

$a/H = 0.05, 0.075, 0.1$ and 0.15, $\rho_r = 2, 10$ and 100, $\Phi_0 = 0.3\%, 0.84\%$ and 2.36%, and $Re_p < 227$. From our results, the following conclusions can be drawn.

(i) At low Re_p, the turbulent intensity across the channel is all diminished; at intermediate Re_p, the turbulent intensity is enhanced in the channel centre region and attenuated in the near-wall region; and at sufficiently large Re_p, the turbulent intensity is enhanced across the channel. The particles attenuate turbulence by suppressing large-scale vortices, which is related to the effect of the drag force distributed in the bulk region; while they enhance turbulence by generating wake vortices, which is related to the interfacial term (i.e. the particle-induced production rate) in the TKE equation. The critical Re_p increases with increasing bulk Reynolds number, particle size and particle–fluid density ratio, while increasing with decreasing particle volume fraction, particularly for the channel centre region. The effects of the bulk Reynolds number, particle size and particle volume fraction on the TKE and critical Re_p can be explained by the dependence of the interfacial term on these parameters (4.14).

(ii) The augmentation of the total TKE in the channel occurs at a value of $\chi_1 = Re_p/[Re_b^{0.33}(d_p/H)^{0.61}\rho_r^{0.05}] > 20$, while attenuation occurs at $\chi_1 < 20$. The augmentation of the TKE at the channel centre occurs at $\chi_2 = \Phi_0^{0.1}Re_p/[Re_b^{0.53}(d_p/H)^{0.61}\rho_r^{0.065}] > 1.55$, while attenuation occurs at $\chi_2 < 1.55$. These two criteria are in good agreement with the previous experimental data.

(iii) The coefficient in the Troshko–Hassan model for the interfacial term is fitted from our DNS data as $C_n = 2.1Re_p^{-0.09}(a/H)^{0.12}\rho_r^{0.007}(1 - \Phi_s)^{8.0}$. The effects of the parameters on C_n may be explained by the effect of the parameters on the particle velocity fluctuation.

(iv) For the particle-laden flows, the wall friction first decreases and then increases as u_i/u_b increases. The decrease in the wall friction for $\rho_r = 2$ is caused by the decrease in the fluid Reynolds stress, and the subsequent increase in C_f is due to the increase in the gravity term C_g or in the fluid Reynolds stress. The attenuation in the fluid Reynolds stress is more pronounced for smaller particles or a lower bulk Reynolds number, since the particle-induced TKE production is more significant for smaller particles or a lower bulk Reynolds number at comparable u_i/u_b. The effect of the gravity term is also more significant for smaller particles or a lower bulk Reynolds number at comparable u_i/u_b. The contribution to the wall friction from the fluid Reynolds stress for $\rho_r = 2$ first decreases and then increases as u_i/u_b increases, whereas it is almost independent of u_i/u_b for $\rho_r = 100$.

(v) At relatively low particle Reynolds numbers, the particles migrate towards the channel centre due to the Saffman effect, whereas at relatively high particle Reynolds numbers, the fluid mean velocity and the particle concentration distribution are almost uniform in the bulk region, and a peak of the particle concentration distribution appears in the near-wall region. The peak position shifts closer to the wall as the particle Reynolds number increases. The peak position is well correlated with the trough (local minimum) of the particle r.m.s. velocity component in the wall-normal direction, as well as the fluid r.m.s. velocity components.

We believe that the present work enhances significantly the understanding of the modulation of the TKE by the spherical particles. However, it is not clear whether our criteria are valid for parameters far beyond the range studied, such as the situation at high bulk Reynolds numbers. The particle modulation of the turbulence intensity in a wider

parameter range for upward channel flow and for other flows such as downward channel flow and jet flows is worth studying. The drag and lift models, the RANS model and the second-order model for particle-laden turbulent flows based on the IR-DNS data are good subjects for extensive future work.

Author ORCIDs.
Zhaosheng Yu https://orcid.org/0000-0001-8999-407X;
Yu Guo https://orcid.org/0000-0002-0012-4498.

REFERENCES

ANSYS, INC. 2013 *ANSYS FLUENT Theory Guide. Release 15.0*. Canonsburg.
ARDEKANI, M.N., COSTA, P., BREUGEM, W.-P., PICANO, F. & BRANDT, L. 2017 Drag reduction in turbulent channel flow laden with finite-size oblate spheroids. *J. Fluid Mech.* **816**, 43–70.
AUTON, T.R. 1987 The lift force on a spherical body in a rotational flow. *J. Fluid Mech.* **183**, 199–218.
AUTON, T.R., HUNT, J.C.R. & PRUD'HOMME, M. 1988 The force exerted on a body in inviscid unsteady non-uniform rotational flow. *J. Fluid Mech.* **197**, 241–257.
BALACHANDAR, S. & EATON, J.K. 2010 Turbulent dispersed multiphase flow. *Annu. Rev. Fluid Mech.* **42**, 111–133.
BARNOCKY, G. & DAVIS, R.H. 1988 Elastohydrodynamic collision and rebound of spheres: experimental verification. *Phys. Fluids* **31** (6), 1324–1329.
BELLANI, G., BYRON, M.L., COLLIGNON, A.G., MEYER, C.R. & VARIANO, E.A. 2012 Shape effects on turbulent modulation by large nearly neutrally buoyant particles. *J. Fluid Mech.* **712**, 41–60.
BIEGERT, E., VOWINCKEL, B. & MEIBURG, E. 2017 A collision model for grain-resolving simulations of flows over dense, mobile, polydisperse granular sediment beds. *J. Comput. Phys.* **340**, 105–127.
BRÄNDLE DE MOTTA, J.C., BREUGEM, W.-P., GAZANION, B., ESTIVALEZES, J.-L., VINCENT, S. & CLIMENT, E. 2013 Numerical modelling of finite-size particle collisions in a viscous fluid. *Phys. Fluids* **25** (8), 083302.
CAPORALONI, M., TAMPIERI, F., TROMBETTI, F. & VITTORI, O. 1975 Transfer of particles in nonisotropic air turbulence. *J. Atmos. Sci.* **32** (3), 565–568.
CLIFT, R., GRACE, J.R. & WEBER, M.E. 2005 *Bubbles, Drops, and Particles*. Courier Corporation.
COSTA, P., BOERSMA, B.J., WESTERWEEL, J. & BREUGEM, W.-P. 2015 Collision model for fully resolved simulations of flows laden with finite-size particles. *Phys. Rev.* E **92** (5), 053012.
COSTA, P., BRANDT, L. & PICANO, F. 2020 Interface-resolved simulations of small inertial particles in turbulent channel flow. *J. Fluid Mech.* **883**, A54.
COSTA, P., PICANO, F., BRANDT, L. & BREUGEM, W.-P. 2018 Effects of the finite particle size in turbulent wall-bounded flows of dense suspensions. *J. Fluid Mech.* **843**, 450–478.
CROWE, C.T. 2000 On models for turbulence modulation in fluid–particle flows. *Intl J. Multiphase Flow* **26** (5), 719–727.
CROWE, C.T., SCHWARZKOPF, J.D., SOMMERFELD, M. & TSUJI, Y. 2011 *Multiphase Flows with Droplets and Particles*. CRC Press.
EATON, J.K. 2009 Two-way coupled turbulence simulations of gas-particle flows using point-particle tracking. *Intl J. Multiphase Flow* **35** (9), 792–800.
ELGHOBASHI, S. & TRUESDELL, G.C. 1993 On the two-way interaction between homogeneous turbulence and dispersed solid particles. I: turbulence modification. *Phys. Fluids* A*: Fluid Dyn.* **5** (7), 1790–1801.
FORNARI, W., FORMENTI, A., PICANO, F. & BRANDT, L. 2016 The effect of particle density in turbulent channel flow laden with finite size particles in semi-dilute conditions. *Phys. Fluids* **28** (3), 033301.
FORNARI, W., KAZEROONI, H.T., HUSSONG, J. & BRANDT, L. 2018 Suspensions of finite-size neutrally buoyant spheres in turbulent duct flow. *J. Fluid Mech.* **851**, 148–186.
FUKAGATA, K., IWAMOTO, K. & KASAGI, N. 2002 Contribution of Reynolds stress distribution to the skin friction in wall-bounded flows. *Phys. Fluids* **14** (11), L73–L76.
GAO, H., LI, H. & WANG, L.-P. 2013 Lattice Boltzmann simulation of turbulent flow laden with finite-size particles. *Comput. Maths Applics.* **65** (2), 194–210.

Garcia-Villalba, M., Kidanemariam, A.G. & Uhlmann, M. 2012 DNS of vertical plane channel flow with finite-size particles: Voronoi analysis, acceleration statistics and particle-conditioned averaging. *Intl J. Multiphase Flow* **46**, 54–74.

Glowinski, R., Pan, T.-W., Hesla, T.I. & Joseph, D.D. 1999 A distributed lagrange multiplier/fictitious domain method for particulate flows. *Intl J. Multiphase Flow* **25** (5), 755–794.

Goes Oliveira, J.L., van der Geld, C.W.M. & Kuerten, J.G.M. 2017 Concentration and velocity statistics of inertial particles in upward and downward pipe flow. *J. Fluid Mech.* **822**, 640–663.

Gondret, P., Lance, M. & Petit, L. 2002 Bouncing motion of spherical particles in fluids. *Phys. Fluids* **14** (2), 643–652.

Gore, R.A. & Crowe, C.T. 1989 Effect of particle size on modulating turbulent intensity. *Intl J. Multiphase Flow* **15** (2), 279–285.

Hertz, H.R. 1882 Uber die beruhrung fester elastischer korper und uber die harte. In *Verhandlung des Vereins zur Beforderung des Gewerbefleißes, Berlin* p. 449. Duncker.

Hetsroni, G. 1989 Particles-turbulence interaction. *Intl J. Multiphase Flow* **15** (5), 735–746.

Hosokawa, S. & Tomiyama, A. 2004 Turbulence modification in gas–liquid and solid–liquid dispersed two-phase pipe flows. *Intl J. Heat Fluid Flow* **25** (3), 489–498.

Hosokawa, S. & Tomiyama, A. 2009 Multi-fluid simulation of turbulent bubbly pipe flows. *Chem. Engng Sci.* **64** (24), 5308–5318.

Hoyas, S. & Jiménez, J. 2008 Reynolds number effects on the Reynolds-stress budgets in turbulent channels. *Phys. Fluids* **20** (10), 101511.

Jeffrey, D.J. 1982 Low-Reynolds-number flow between converging spheres. *Mathematika* **29** (1), 58–66.

Kajishima, T., Takiguchi, S., Hamasaki, H. & Miyake, Y. 2001 Turbulence structure of particle-laden flow in a vertical plane channel due to vortex shedding. *JSME Intl J. Ser.* B *Fluids Therm. Engng* **44** (4), 526–535.

Kempe, T. & Fröhlich, J. 2012 Collision modelling for the interface-resolved simulation of spherical particles in viscous fluids. *J. Fluid Mech.* **709**, 445–489.

Kiger, K.T. & Pan, C. 2002 Suspension and turbulence modification effects of solid particulates on a horizontal turbulent channel flow. *J. Turbul.* **3** (19), 1–17.

Kulick, J.D., Fessler, J.R. & Eaton, J.K. 1994 Particle response and turbulence modification in fully developed channel flow. *J. Fluid Mech.* **277**, 109–134.

Kussin, J. & Sommerfeld, M. 2002 Experimental studies on particle behaviour and turbulence modification in horizontal channel flow with different wall roughness. *Exp. Fluids* **33** (1), 143–159.

Lee, S.L. & Durst, F. 1982 On the motion of particles in turbulent duct flows. *Intl J. Multiphase Flow* **8** (2), 125–146.

Li, Y., McLaughlin, J.B., Kontomaris, K. & Portela, L. 2001 Numerical simulation of particle-laden turbulent channel flow. *Phys. Fluids* **13** (10), 2957–2967.

Lin, Z.-W., Shao, X.-M., Yu, Z.-S. & Wang, L.-P. 2017*b* Effects of finite-size heavy particles on the turbulent flows in a square duct. *J. Hydrodyn.* **29** (2), 272–282.

Lin, Z., Yu, Z., Shao, X. & Wang, L.-P. 2017*a* Effects of finite-size neutrally buoyant particles on the turbulent flows in a square duct. *Phys. Fluids* **29** (10), 103304.

Liu, C., Tang, S., Shen, L. & Dong, Y. 2017 Characteristics of turbulence transport for momentum and heat in particle-laden turbulent vertical channel flows. *Acta Mechanica Sin.* **33** (5), 833–845.

Lucci, F., Ferrante, A. & Elghobashi, S. 2010 Modulation of isotropic turbulence by particles of Taylor length-scale size. *J. Fluid Mech.* **650**, 5–55.

Luo, K., Luo, M. & Fan, J. 2016 On turbulence modulation by finite-size particles in dilute gas-solid internal flows. *Powder Technol.* **301**, 1259–1263.

Ma, T., Lucas, D., Jakirlić, S. & Fröhlich, J. 2020 Progress in the second-moment closure for bubbly flow based on direct numerical simulation data. *J. Fluid Mech.* **883**, A9.

Ma, T., Santarelli, C., Ziegenhein, T., Lucas, D. & Fröhlich, J. 2017 Direct numerical simulation–based Reynolds-averaged closure for bubble-induced turbulence. *Phys. Rev. Fluids* **2** (3), 034301.

Maeda, M., Hishida, K. & Furutani, T. 1980 Velocity distributions of air-solids suspension in upward pipe flow: effect of particles on air velocity distribution. In *Transactions of the Japan Society of Mechanical Engineers, Series B*, vol. 46 (412), pp. 2313–2320. Japan Society of Mechanical Engineers.

Maxey, M. 2017 Simulation methods for particulate flows and concentrated suspensions. *Annu. Rev. Fluid Mech.* **49**, 171–193.

Mena, S.E. & Curtis, J.S. 2020 Experimental data for solid–liquid flows at intermediate and high stokes numbers. *J. Fluid Mech.* **883**, A24.

Mindlin, R.D. 1953 Elastic spheres in contact under varying oblique forces. *J. Appl. Mech.* **20**, 327–344.

MURAMULLA, P., TYAGI, A., GOSWAMI, P.S. & KUMARAN, V. 2020 Disruption of turbulence due to particle loading in a dilute gas–particle suspension. *J. Fluid Mech.* **889**, A28.

NOGUCHI, K. & NEZU, I. 2009 Particle–turbulence interaction and local particle concentration in sediment-laden open-channel flows. *J. Hydro-Environ. Res.* **3** (2), 54–68.

PARTHASARATHY, R.N. & FAETH, G.M. 1990 Turbulence modulation in homogeneous dilute particle-laden flows. *J. Fluid Mech.* **220**, 485–514.

PENG, C., AYALA, O.M. & WANG, L.-P. 2019 A direct numerical investigation of two-way interactions in a particle-laden turbulent channel flow. *J. Fluid Mech.* **875**, 1096–1144.

PENG, C. & WANG, L.-P. 2019 Direct numerical simulations of turbulent pipe flow laden with finite-size neutrally buoyant particles at low flow Reynolds number. *Acta Mechanica* **230** (2), 517–539.

PETERSEN, A.J., BAKER, L. & COLETTI, F. 2019 Experimental study of inertial particles clustering and settling in homogeneous turbulence. *J. Fluid Mech.* **864**, 925–970.

PICANO, F., BREUGEM, W.-P. & BRANDT, L. 2015 Turbulent channel flow of dense suspensions of neutrally buoyant spheres. *J. Fluid Mech.* **764**, 463–487.

REEKS, M.W. 1983 The transport of discrete particles in inhomogeneous turbulence. *J. Aerosol Sci.* **14** (6), 729–739.

RIGHETTI, M. & ROMANO, G.P. 2004 Particle–fluid interactions in a plane near-wall turbulent flow. *J. Fluid Mech.* **505**, 93–121.

SABER, A., LUNDSTRÖM, T.S. & HELLSTRÖM, J.G.I. 2015 Turbulent modulation in particulate flow: a review of critical variables. *Engineering* **7** (10), 597.

SAFFMAN, P.G.T. 1965 The lift on a small sphere in a slow shear flow. *J. Fluid Mech.* **22** (2), 385–400.

SAITO, I., WATANABE, T. & GOTOH, T. 2019 A new time scale for turbulence modulation by particles. *J. Fluid Mech.* **880**, R6.

SANTARELLI, C. & FRÖHLICH, J. 2015 Direct numerical simulations of spherical bubbles in vertical turbulent channel flow. *Intl J. Multiphase Flow* **75**, 174–193.

SANTARELLI, C., ROUSSEL, J. & FRÖHLICH, J. 2016 Budget analysis of the turbulent kinetic energy for bubbly flow in a vertical channel. *Chem. Engng Sci.* **141**, 46–62.

SATO, Y. & HISHIDA, K. 1996 Transport process of turbulence energy in particle-laden turbulent flow. *Intl J. Heat Fluid Flow* **17** (3), 202–210.

SCHRECK, S. & KLEIS, S.J. 1993 Modification of grid-generated turbulence by solid particles. *J. Fluid Mech.* **249**, 665–688.

SERIZAWA, A., KATAOKA, I. & MICHIYOSHI, I. 1975 Turbulence structure of air-water bubbly flow-II. Local properties. *Intl J. Multiphase Flow* **2** (3), 235–246.

SHAO, X., WU, T. & YU, Z. 2012 Fully resolved numerical simulation of particle-laden turbulent flow in a horizontal channel at a low Reynolds number. *J. Fluid Mech.* **693**, 319–344.

SHOKRI, R., GHAEMI, S., NOBES, D.S. & SANDERS, R.S. 2017 Investigation of particle-laden turbulent pipe flow at high-Reynolds-number using particle image/tracking velocimetry (piv/ptv). *Intl J. Multiphase Flow* **89**, 136–149.

SQUIRES, K.D. & EATON, J.K. 1990 Particle response and turbulence modification in isotropic turbulence. *Phys. Fluids* A*: Fluid Dyn.* **2** (7), 1191–1203.

SUZUKI, Y., IKENOYA, M. & KASAGI, N. 2000 Simultaneous measurement of fluid and dispersed phases in a particle-laden turbulent channel flow with the aid of 3-D PTV. *Exp. Fluids* **29** (1), S185–S193.

TANAKA, T. & EATON, J.K. 2008 Classification of turbulence modification by dispersed spheres using a novel dimensionless number. *Phys. Rev. Lett.* **101** (11), 114502.

TEN CATE, A., DERKSEN, J.J., PORTELA, L.M. & VAN DEN AKKER, H.E.A. 2004 Fully resolved simulations of colliding monodisperse spheres in forced isotropic turbulence. *J. Fluid Mech.* **519**, 233–271.

TENNETI, S. & SUBRAMANIAM, S. 2014 Particle-resolved direct numerical simulation for gas-solid flow model development. *Annu. Rev. Fluid Mech.* **46**, 199–230.

THEOFANOUS, T.G. & SULLIVAN, J. 1982 Turbulence in two-phase dispersed flows. *J. Fluid Mech.* **116**, 343–362.

TROSHKO, A.A. & HASSAN, Y.A. 2001 A two-equation turbulence model of turbulent bubbly flows. *Intl J. Multiphase Flow* **27** (11), 1965–2000.

TSUJI, Y. & MORIKAWA, Y. 1982 LDV measurements of an air—solid two-phase flow in a horizontal pipe. *J. Fluid Mech.* **120**, 385–409.

TSUJI, Y., MORIKAWA, Y. & SHIOMI, H. 1984 LDV measurements of an air-solid two-phase flow in a vertical pipe. *J. Fluid Mech.* **139**, 417–434.

TSUJI, Y., TANAKA, T. & ISHIDA, T. 1992 Lagrangian numerical simulation of plug flow of cohesionless particles in a horizontal pipe. *Powder Technol.* **71** (3), 239–250.

UHLMANN, M. 2008 Interface-resolved direct numerical simulation of vertical particulate channel flow in the turbulent regime. *Phys. Fluids* **20** (5), 053305.

VREMAN, A.W. 2015 Turbulence attenuation in particle-laden flow in smooth and rough channels. *J. Fluid Mech.* **773**, 103–136.

VREMAN, A.W. & KUERTEN, J.G.M. 2018 Turbulent channel flow past a moving array of spheres. *J. Fluid Mech.* **856**, 580–632.

WANG, B. 2010 Inter-phase interaction in a turbulent, vertical channel flow laden with heavy particles. Part II: two-phase velocity statistical properties. *Intl J. Heat Mass Transfer* **53** (11-12), 2522–2529.

WANG, G., ABBAS, M. & CLIMENT, É. 2017 Modulation of large-scale structures by neutrally buoyant and inertial finite-size particles in turbulent Couette flow. *Phys. Rev. Fluids* **2** (8), 084302.

WANG, G., FONG, K.O., COLETTI, F., CAPECELATRO, J. & RICHTER, D.H. 2019 Inertial particle velocity and distribution in vertical turbulent channel flow: a numerical and experimental comparison. *Intl J. Multiphase Flow* **120**, 103105.

WANG, L.-P. & MAXEY, M.R. 1993 Settling velocity and concentration distribution of heavy particles in homogeneous isotropic turbulence. *J. Fluid Mech.* **256**, 27–68.

WANG, L.-P., PENG, C., GUO, Z. & YU, Z. 2016 Flow modulation by finite-size neutrally buoyant particles in a turbulent channel flow. *J. Fluids Engng* **138** (4), 041306.

WU, T.-H., SHAO, X.-M. & YU, Z.-S. 2011 Fully resolved numerical simulation of turbulent pipe flows laden with large neutrally-buoyant particles. *J. Hydrodyn.* **23** (1), 21–25.

XIA, Y., XIONG, H., YU, Z. & ZHU, C. 2020*a* Effects of the collision model in interface-resolved simulations of particle-laden turbulent channel flows. *Phys. Fluids* **32** (10), 103303.

XIA, Y., YU, Z. & DENG, J. 2019 A fictitious domain method for particulate flows of arbitrary density ratio. *Comput. Fluids* **193**, 104293.

XIA, Y., YU, Z. & GUO, Y. 2020*b* Interface-resolved numerical simulations of particle-laden turbulent channel flows with spanwise rotation. *Phys. Fluids* **32** (1), 013303.

YU, Z., LIN, Z., SHAO, X. & WANG, L.-P. 2016*b* A parallel fictitious domain method for the interface-resolved simulation of particle-laden flows and its application to the turbulent channel flow. *Engng Appl. Comput. Fluid Mech.* **10** (1), 160–170.

YU, Z., LIN, Z., SHAO, X. & WANG, L.-P. 2017 Effects of particle-fluid density ratio on the interactions between the turbulent channel flow and finite-size particles. *Phys. Rev.* E **96** (3), 033102.

YU, Z., PHAN-THIEN, N. & TANNER, R.I. 2004 Dynamic simulation of sphere motion in a vertical tube. *J. Fluid Mech.* **518**, 61–93.

YU, Z. & SHAO, X. 2007 A direct-forcing fictitious domain method for particulate flows. *J. Comput. Phys.* **227** (1), 292–314.

YU, W., VINKOVIC, I. & BUFFAT, M. 2016*a* Finite-size particles in turbulent channel flow: quadrant analysis and acceleration statistics. *J. Turbul.* **17** (11), 1048–1071.

YU, Z., ZHU, C., WANG, Y. & SHAO, X. 2019 Effects of finite-size neutrally buoyant particles on the turbulent channel flow at a Reynolds number of 395. *Appl. Maths Mech.* **40** (2), 293–304.

ZADE, S., LUNDELL, F. & BRANDT, L. 2019 Turbulence modulation by finite-size spherical particles in newtonian and viscoelastic fluids. *Intl J. Multiphase Flow* **112**, 116–129.

ZHAO, L.H., ANDERSSON, H.I. & GILLISSEN, J.J.J. 2010 Turbulence modulation and drag reduction by spherical particles. *Phys. Fluids* **22** (8), 081702.

ZHAO, L., ANDERSSON, H.I. & GILLISSEN, J.J.J. 2013 Interphasial energy transfer and particle dissipation in particle-laden wall turbulence. *J. Fluid Mech.* **715**, 32–59.

ZHU, H.-Y., PAN, C., WANG, J.-J., LIANG, Y.-R. & JI, X.-C. 2019 Sand-turbulence interaction in a high-Reynolds-number turbulent boundary layer under net sedimentation conditions. *Intl J. Multiphase Flow* **119**, 56–71.

ZHU, C., YU, Z., PAN, D. & SHAO, X. 2020*a* Interface-resolved direct numerical simulations of the interactions between spheroidal particles and upward vertical turbulent channel flows. *J. Fluid Mech.* **891**, A6.

ZHU, C., YU, Z. & SHAO, X. 2018 Interface-resolved direct numerical simulations of the interactions between neutrally buoyant spheroidal particles and turbulent channel flows. *Phys. Fluids* **30** (11), 115103.

ZHU, C., YU, Z., SHAO, X. & DENG, J. 2020*b* Interface-resolved numerical simulations of particle-laden turbulent flows in a vertical channel filled with Bingham fluids. *J. Fluid Mech.* **883**, A43.